Frequency stabilization of a laser and a high resolution optical setup for excitation of ultracold Rydberg atoms

Samuel Germer

Bachelorarbeit in Physik
angefertigt im Institut für Angewandte Physik

vorgelegt der
Mathematisch-Naturwissenschaftlichen Fakultät
der
Rheinischen Friedrich-Wilhelms-Universität
Bonn

August 2023

Ich versichere, dass ich diese Arbeit selbstständig verfasst und keine anderen als die angegebenen Quellen und Hilfsmittel benutzt sowie die Zitate kenntlich gemacht habe.

Bonn, 10.08.2023 .....
Datum

.....
Unterschrift

1. Gutachter: Prof. Dr. Sebastian Hofferberth
2. Gutachter: Prof. Dr. Stefan Linden

Acknowledgements

I would like to thank all the members of the Nonlinear Quantum Optics group who have been super nice and helpful in all regards. It was super fun to be part of the group. I would like to thank all of the members from the HQO experiment, especially Hannes Busche, Julia Gamper and Cedric Wind for everyday support. Thanks to Nina and Lukas from RQO and Thilina from YQO for Proofreading and giving me very helpful feedback. Also, thanks to all the other people who read my thesis and gave me feedback. Finally, I would like to thank my family who always supports me.

Contents

1 Introduction **1**

2 Laser system **3**
2.1 Laser setup of the experiment . . . 3
2.2 Probe light at 780 nm . . . 4
2.3 Control light at 480 nm . . . 6
2.3.1 Frequency Stabilization . . . 6
2.3.2 Acousto-optic modulator . . . 9

3 Arducam MT9J001 for beam characterization **11**
3.1 The camera . . . 11
3.2 Calibration . . . 12
3.2.1 Customizing the camera gain settings . . . 14
3.2.2 Calibration for 780 nm light . . . 16
3.2.3 Calibration for 480 nm light and conclusion . . . 17
3.3 Software for beam-profiling and alignment . . . 20

4 Optic setup for excitation of Rydberg atoms in 1D-geometry **22**
4.1 Gaussian beams . . . 22
4.2 Requirements for the setup . . . 23
4.3 Design . . . 26
4.3.1 Probe beam . . . 26
4.3.2 Control beam . . . 26
4.4 Assembly of the setup . . . 27
4.4.1 Probe-beam . . . 27
4.4.2 Control-beam . . . 36

5 Summary and outlook **39**

A Appendix **41**
A.1 Useful tools - microscope . . . 41
A.2 Placement of second lens to optimize the coupling efficiency . . . 44
A.3 Arducam . . . 45
A.3.1 Distortion of beam profile by the camera . . . 45
A.3.2 Code of software for alignment and beam profiling . . . 45

Bibliography 49

CHAPTER 1

Introduction

Many of today's promising platforms for quantum computation operates with microwave qubits [1]. However, microwave photons are not ideal for sending over long distances. Photons in the optical regime are more convenient, because there is basically no optical background and they can be transmitted through conventional optical fibers. Therefore, it is very attractive to find ways of interfacing microwave and optical systems. Rydberg atoms, which are highly excited atoms, are an ideal candidate for such hybrid systems, because their transition cover a wide range of the electro-magnetic spectrum from the optical range to microwaves [2]. This allows them to interact with quantum systems in either domain. In the microwave regime, they are one of the most sensitive antennas for microwave fields due to the strong transitions between neighboring Rydberg states [3] [4].

In the HQO (Hybrid Quantum Optics) experiment, we plan to use these properties of Rydberg atoms to bring them into interaction with an electromechanical acoustic oscillator [5] [6]. These oscillators are a novel platform to study mesoscopic quantum systems and are typically interfaced with superconducting qubits[7].

To study the interaction in a regime where the quantum nature of the oscillator becomes apparent, a 4 K environment inside a cryostat is required [8] [9]. One goal is to cool an oscillator mode into its ground state by extracting phonons via the interaction with the atoms.

Another important feature of ultracold Rydberg atoms is the blockade effect that results from the strong dipolar interactions between them. This effect suppresses multiple excitations within a blockade radius of order 10 µm around the excited atom [10]. This property will be used in the experiment to get an effectively one-dimensional chain of Rydberg atoms above the oscillator as we excite them in a cigar-shaped atom cloud that is magnetically trapped using a superconducting atom chip with a z-wire geometry [11]. This way, one has a well defined distance between the atoms and the oscillator and the coupling strength between them can be controlled by moving the atoms relative to the oscillator. Figure 1.1 shows the planned design of the experiment.

To achieve such an one-dimensional geometry, the laser beams used for Rydberg excitation must be tightly focused such that the beam waist at the focus is below the blockade radius and Rydberg atoms can be excited only along the optical axis. In the HQO experiment, two lasers at 780 nm and 480 nm counter-propagating on a common optical axis will be used for the excitation of ^{87}Rb Rydberg atoms. This is a common scheme for Rydberg excitation, where the 780 nm laser is used to excite to an intermediate state while the 480 nm laser is used to excite to the Rydberg state from there. Such a three-level scheme also allows to study non-linear quantum optics using electro-

magnetically induced transparency [12] [13], e.g. to interface the oscillator with optical photons at later stage . Such a setup has already been successfully implemented in another experiment of the group [14] and will form the basis of the optical setup for Rydberg excitation in the HQO experiment.

Another important aspect is the linewidth of the excitation lasers. If the linewidths become comparable to the interaction-induced energy shifts between Rydberg states (of order MHz), the blockade effect breaks down. But to suppress decoherence of the Rydberg excited atoms, much lower linewidths of order kHz comparable to the natural lifetime of Rydberg states are desirable.

In this thesis the implementation of the laser system and optical setup for Rydberg excitation is realized and characterized. In chapter 2, the 480 nm laser (one of the two excitation lasers) is frequency stabilized to a ultrastable resonator using the Pound-Drever-Hall technique to achieve a narrow linewidth of a few kHz. Furthermore, for both lasers, acousto-optical modulators are installed to act as fast switches for the excitation pulses. The lasers are thus prepared and the light can be sent through fibers to the experiment where the excitation happens.
The laser system for Rydberg excitation contains two lasers, which both have to be focused very tightly to address the atoms in a 1D geometry. The characterization of beam focusing requires a suitable beam-imaging technique. Therefore, chapter 3 presents how to calibrate and use the *Arducam MT9J001*, a commercial camera with a small pixel size of 1.67 µm x 1.67 µm [15] for beam characterization.
In chapter 4, the optical setup for the Rydberg excitation in the actual experiment is built and tested. In section 4.2, the requirements for the setup to achieve the one dimensional excitation geometry are discussed. The final setup is presented in section 4.3. Section 4.4 discusses the assembly and characterization of the test setup. This way it is ensured that the requirements from section 4.2 are met and that both beams have a Gaussian profile [16] without any abberations.

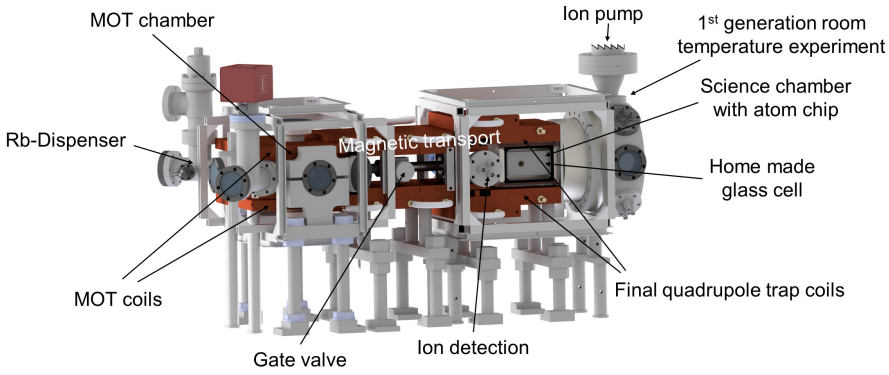

Figure 1.1: Design of the HQO experimet. Atoms will be cooled and trapped with the MOT. Then, the magnetic transport will bring them to the atom chip inside the science chamber. There, the atoms will be trapped above the mechanical oscillator on the chip and excited to a Rydberg state. Courtesy of Cedric Wind

CHAPTER 2

Laser system

Creating Rydberg excitations require the relevant lasers to address the atoms. The lasers need to be frequency stabilized to the precision of the Rydberg lines of interest.
Therefore, the laser system of the HQO experiment is presented here. The Pound Drever Hall technique for frequency stabilization is explained and used to stabilize the 480 nm laser for Rydberg excitation. For both excitation lasers, acousto-optical modulators are installed and characterized.

2.1 Laser setup of the experiment

For the preparation and excitation of the atoms, multiple lasers are needed. First, the atoms have to be cooled and trapped. The laser setup for this is described in the bachelor thesis of Valerie Mauth [17]. After the atoms are cooled and trapped, they will get excited to the Rydberg state. In this experiment, this will be done with a two-photon excitation with a 780 nm and a 480 nm laser. As shown in Figure 2.1, the 780 nm laser is used to get from the $5^2S_{1/2}$ state to the $5^2P_{3/2}$ state [18]. The blue 480 nm laser is then used to go from there to the $n^2S_{1/2}$ Rydberg state (or $n^2D_{5/2}$ / $n^2D_{3/2}$ soon). In the following, the 780 nm laser is named *probe beam* and the 480 nm laser is named *control beam*.

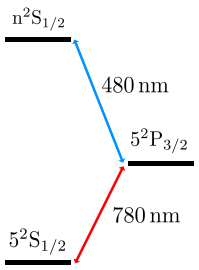

Figure 2.1: LevelScheme of the three states involved in the Rydberg excitation for Rubidium-87, $n \gg 1$

Next, the actual setup of the two lasers will be discussed, which can be seen in Figure 2.2. The two lasers are from *Toptica*. In the final setup of the experiment, a diode laser will be used for the probe light. Because this laser was not available at this time, the non amplified side-output of a

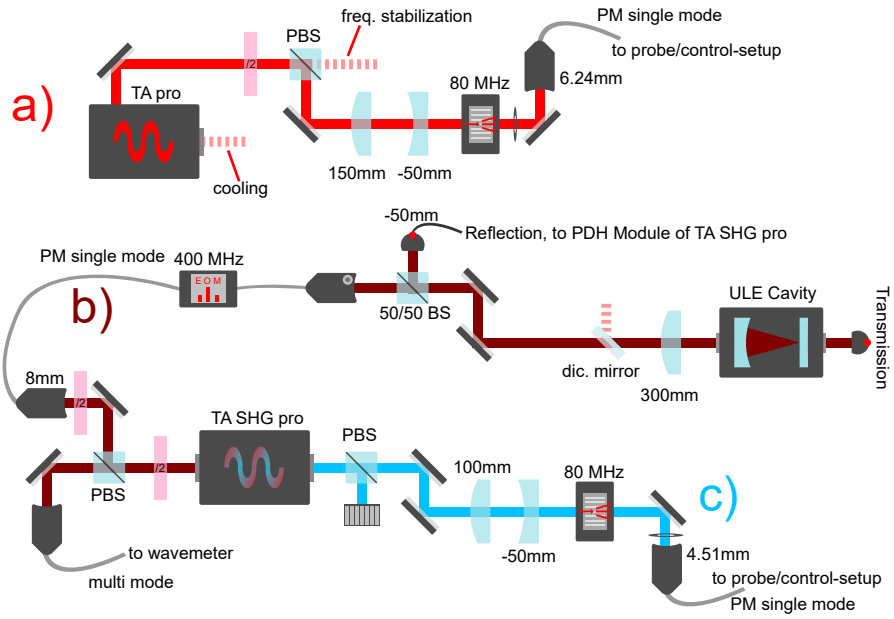

Figure 2.2: sketch of the laser setup of this thesis, a) is for the 780 nm probe light, b) is for the frequency stabilization of the 480 nm laser, c) is for the 480 nm control light

TA-laser (tapered amplifier) was used (the TA is also used for the cooling of the atoms). For the control light, the *TA-SHG pro* is used. The laser consists of an amplified diode laser at 960 nm and a doubling stage. The 960 nm laser is used in littrow configuration, the grating can be moved with a piezo to change the laser frequency. Inside the doubling cavity, 480 nm laser light is produced via second harmonic generation [16]. The laser has a side-output where a fraction of the 960 nm light from the diode is available. This output is used in section 2.3.1 for the frequency stabilization of the laser.

2.2 Probe light at 780 nm

The frequency lock of the 780nm probe laser has already been done by Julia Gamper [19] and Valerie Mauth [17].
Before the laser beam is fiber-coupled, the AOM (acousto optical modulator) *3080-122* from *Gooch & Housego* is installed. This is done because in the planned experiments, the Rydberg excitation will take place in pulses. Therefore it is necessary to be able to switch both probe and control lasers off quickly. For this, acousto-optical modulators are used. The optical setup for this is shown in Figure 2.2.
An AOM has a crystal and a piezo in it. With a home build RF source (using a DDs-source and a series of RF switches, mixers and amplifiers) and the piezo, one can create a sound wave that travels through the crystal. If light passes through the AOM, the light gets diffracted into different orders m at

different angles α_m because of the periodicity of the refractive index caused by the sound wave [20].[1] By tuning the power of the RF-source one can transmit most of the light into the first order (here, around 85 % were reached, this agrees with the manufacturer's specifications [21]).
In order to characterize the property of the AOM as a switch, the rise time and fall time were determined because they are important to know since they determine how fast one can switch the laser on and off. To measure them, the intensity of the laser light after the AOM was detected on a photo diode.
The signal is shown in Figure 2.3(a) for rise time and in Figure 2.3(b) for fall time. The integral of a one dimensional Gaussian beam is fitted to the signal of the photo diode. This is done under the assumption that the beam before the AOM is well described by a Gaussian beam,

$$I_{\text{rise}}(t) = A\frac{1}{2} \cdot \left(1 + \text{erf}\left(\frac{(t-t_0)\sqrt{2}}{\tau}\right)\right) + I_{\text{BG}} \tag{2.1}$$

$$I_{\text{fall}}(t) = A\left(-\frac{1}{2} \cdot \left(1 + \text{erf}\left(\frac{(t-t_0)\sqrt{2}}{\tau}\right)\right) + 1\right) + I_{\text{BG}} \tag{2.2}$$

Here, $I(t)$ is the signal of the photo diode, A is the amplitude, I_{BG} is a background offset of the photo diode signal, t_0 is a time offset and τ is given by $\tau = \frac{w}{v_{\text{cristal}}}$, where w is the radius of the beam inside the AOM and v_{cristal} is the velocity of the sound wave in the crystal. For a TeO_2 crystal as in our AOM, the velocity is given by the following value [21]: $v_{\text{crystal}} = 4.2\,\text{mm}/\mu\text{s}$
The fits can be seen in Figure 2.3. The results of the fall and rise time as well as the calculated beam radius can be seen in Table 2.1. The determined values are within the manufacturer's specifications [21] and sufficiently low to allow shaping of the probe pulses in the experiment which are expected to have $\sim 1\,\mu\text{s}$ duration.
In general, the rise time can be further reduced by using a smaller beam diameter in the AOM, but this reduces the efficiency [21].

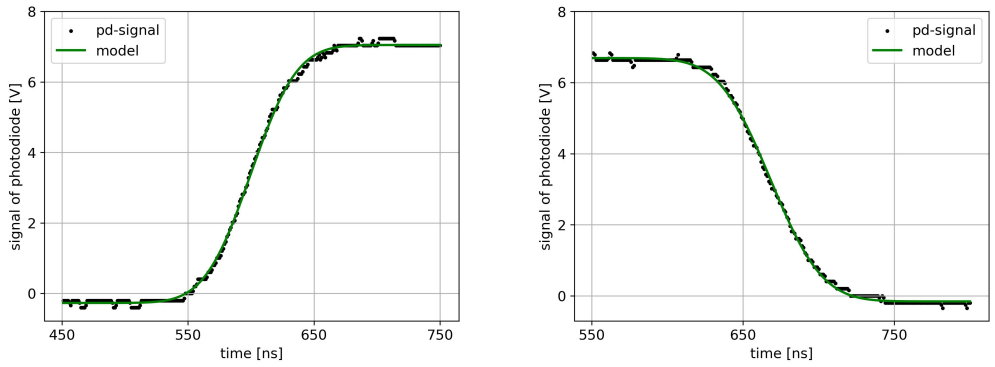

(a) rise time measurement

(b) fall time measurement

Figure 2.3: rise and fall time measurements for the AOM for the probe beam at 780nm

[1] An important point is that the frequency of the laser light is increased by the frequency of the sound wave (in our case 80 MHz). This must be taken into account in the laser lock to a certain transition.

Table 2.1: rise time and fall time and beam radius calculated from fit for probe beam, $t_{90/10}$ is the time within the power rises from 10% to 90% (fall from 90% to 10%)

	$t_{90/10}$ [ns]	beam radius [µm]
fall time measurement	69.2 ± 0.6	242 ± 2
rise time measurement	73.9 ± 0.6	227 ± 2

2.3 Control light at 480 nm

The next section will be about the 480 nm laser which is used to couple from the intermediate state to the Rydberg state. The first part is about the frequency stabilization. In the second part the AOM is installed and characterized as in section 2.2.

2.3.1 Frequency Stabilization

As mentioned in the introduction, the linewidth of the laser must be smaller than the interaction-induced energy shifts between Rydberg atoms (of order MHz) to observe the blockade effect. Furthermore, lower linewidths are desirable to suppress decoherence of the Rydberg excited atom.
Since the laser does not provide such low linewidths out of the box it must be frequency stabilized. In the following, it will be discussed how frequency stabilization works with the Pound Drever Hall (PDH) method [22], and how the laser was frequency stabilized using it.

PDH-Method

In the following, the principle of the PDH method is explained [22].
To stabilize the laser frequency it is necessary to have a stable frequency reference. This reference should have a frequency width small enough to meet the requirements of the experiment. Furthermore, this reference itself must be stable, both on short and long time scales. Here, a ULE-cavity (ultra low expansion) is therefore used as a reference. The laser will be stabilized onto a resonance of the cavity.

To do so, a feedback signal is given back to the laser to counteract any frequency drifting, away from the cavity resonance. To generate this feedback signal, one could either use the transmission or the reflection signal of the cavity. In principle one can recognize drifts by looking at the transmission signal. However, this way one can not distinguish between intensity fluctuations and frequency drifts and it is also not clear in which frequency direction the laser is drifting.
Both problems can be solved by using the reflection signal. At resonance, the reflection signal should be zero, regardless of intensity fluctuations. To determine the direction of the drift, it is used that the phase is antisymetric around the resonance. The PDH method offers a method to measure the phase indirectly and therefore generate such a feedback signal (usually called error signal) for the laser.
Figure 2.4(a) shows such an error signal (theoretical), with zero crossing at resonance and and a linear slope near resonance to determine the direction of frequency drifts. Figure 2.4(b) shows the real error signal in the experiment.

To get such an error signal, an EOM (electro-optic modulator) [23] is used to modulate the phase of

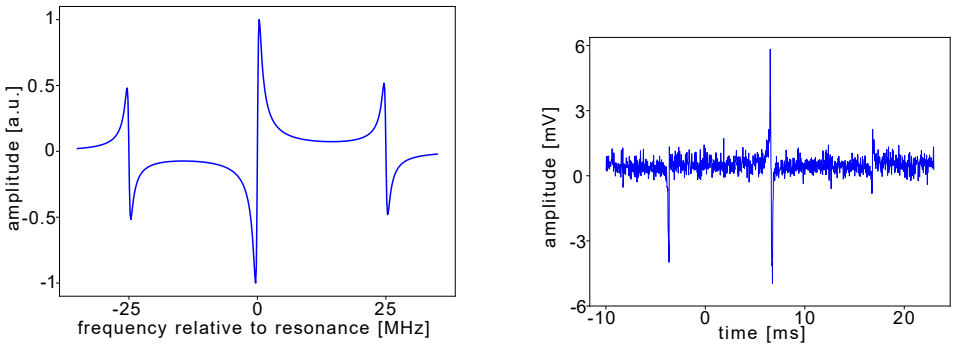

(a) (b)

Figure 2.4: a) Theoretical error signal for modulated 25 MHz sidebands and the given specs of the reference cavity (see (2.5)), the x-axis shows the difference between the carrier frequency of the laser and the frequency of the cavity resonance. b) Error signal at the monitor output of the PID. The laser is scanning the frequency over time, therefore the x-axis is given in ms

the laser light with modulation frequency Ω and amplitude β,

$$E = E_0 \cdot e^{\omega t + \beta \sin \Omega t}\,, \tag{2.3}$$

where E is the electric field of the laser light and ω is the laser frequency.
By applying a phase shift to the modulation signal, mixing it with the measured reflection signal (with a photo diode) and sending it through a low pass filter one can generate the error signal of the following form,

$$\epsilon = -2J_0(\beta)J_1(\beta)P_0\Im\mathfrak{m}\left[F(\omega)\cdot\overline{F(\omega+\Omega)} - \overline{F(\omega)}\cdot F(\omega-\Omega)\right]\,, \tag{2.4}$$

where P_0 is the total intensity of the incident beam, J_0 and J_1 are Bessel functions and $F(\omega)$ is the reflection coefficient of the cavity.
Around resonance, the error signal is linear and can therefore be processed by a PID controller [24]. the output signal from the PID is then applied as a feedback signal to the laser to compensate for frequency drifts.

Setup

The previous section discusses the theory of the PDH. To implement the PDH lock in the experiment, the setup shown in figure 2.5 is used. The 960 nm side-output of the laser is used for frequency stabilization. The modulation of the sidebands for PDH for the lock happens inside the laser box.
Since the transition from the intermediate state to a Rydberg state does not generally coincide with a cavity resonance, microwave sidebands are modulated onto the 960 nm light using a fiber coupled EOM from *EO-Space*. The *Windfreak SynthUSB2* with an amplifier is used as a RF-source. One can then lock the laser onto a sideband. The frequency of the sidebands can be adjusted arbitrarily. This allows the laser to be stabilized at any frequency between two cavity resonances.
After the fiber EOM, the light is coupled into the cavity. The cavity is from *Stable Laser Systems*. The

free spectral range and the finesse were measured by Florian Pausenwang [25]:

$$\Delta\nu_{\mathrm{FSR}} = (1\,492 \pm 43)\,\mathrm{MHz} \tag{2.5}$$

$$\mathcal{F} = 28600 \pm 300 \tag{2.6}$$

Both the transmission and reflection signals are measured with a photo diode. The reflection signal is then applied to the commercial PDH module from *Toptica*. This has the phase shifter, the mixer and the low pass filter built in. After processing the signal, it is given as an error signal to the PID controller (commercial PID controller *Falc 100* from *Toptica*). The output from it is then given as a feedback signal to the laser. The laser compensates for fast drifts by adjusting the laser current and for slow drifts by adjusting the piezo voltage.

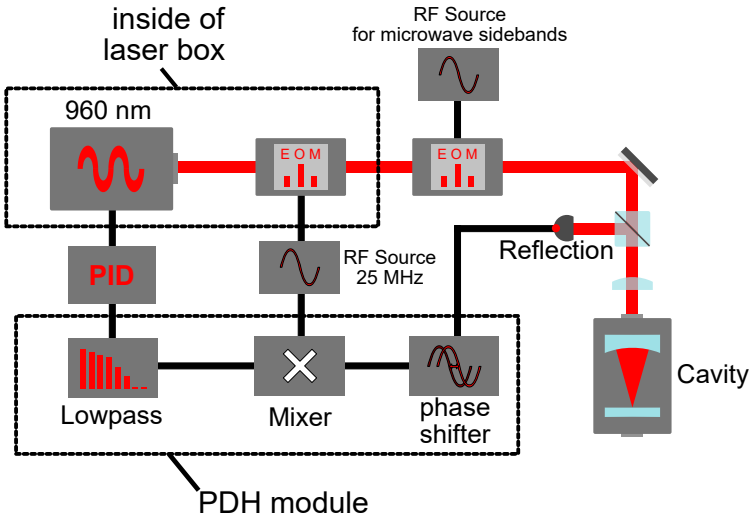

Figure 2.5: Setup for frequency stabilization with the Pound Drever Hall method with modulation of additional microwave sidebands to arbitrarily set the locking point

For a stable lock, the first thing to do is to optimize the coupling into the cavity. Ideally, only the fundamental mode should be coupled in. In reality this means to maximize the ratio between the fundamental mode and higher modes. For this the laser beam must have its focus at the rear mirror of the cavity. At the front mirror, the curvature of the wave fronts must match the curvature of the mirror [16]. The shape of the laser beam is adjusted by a lens in front of the cavity. The lens was already placed by Cedric Wind and Valerie Mauth for stabilization of the 780 nm laser. In order to also couple the 960 nm light into the cavity, the position of the lens for outcoupling from the fiber EOM was adjusted. Higher modes could be suppressed to slightly less than one percent of the fundamental mode.

With an optimized cavity coupling, the locking parameters could be optimized. This is necessary to increase the stability of the lock and minimize the lindewidth of the laser.
Two parameters determine the quality of the error-signal, namely the phase and the offset. The offset is adjusted such that the error signal is centered around zero, and the phase is adjusted by maximizing the slope of the error signal.
The quality of the lock can be judged by the error signal in the locked state and the frequency spectrum

of the error signal (measured with a spectrum analyzer) and the transmission amplitude. In the locked state, the fluctuations of the error signal should be as small as possible. In the frequency domain, one sees an bump in the spectrum, this is called a servo bump. The locking parameters should be chosen such that the noise is suppressed at all frequencies, and such that the servo-bump is pushed to the highest possible frequencies. This then means that the PID does not have to react strongly to drifts but the PID reacts quickly. Furthermore, the transmission amplitude should be maximal and stable.
Figure 2.6 shows the frequency spectrum of the error signal before and after optimization (the peak at 750 kHz is a signal that was picked up by the cables). One can see that the servo-bump was suppressed and shifted to the right. The main gain was adjusted until the peak-to-peak amplitude of the error signal was minimal.

By comparing the slope of the error signal when the laser is not locked with the peak to peak amplitude of the error signal when the laser is locked one can estimate the linewidth of the laser. The scan with the main laser frequency and a microwave sideband at 400 MHz provides a frequency ruler to convert the time axis to a frequency axis. From these measurement a linewidth $\Delta\nu$ of about

$$\Delta\nu \approx 3\,\text{kHz} \tag{2.7}$$

could be estimated. Florian Pausenwang achieved a linewidth of about 1 kHz [25] with a more precise measurement method. This measurement provides a rough estimation of the linewidth which is of the same order.

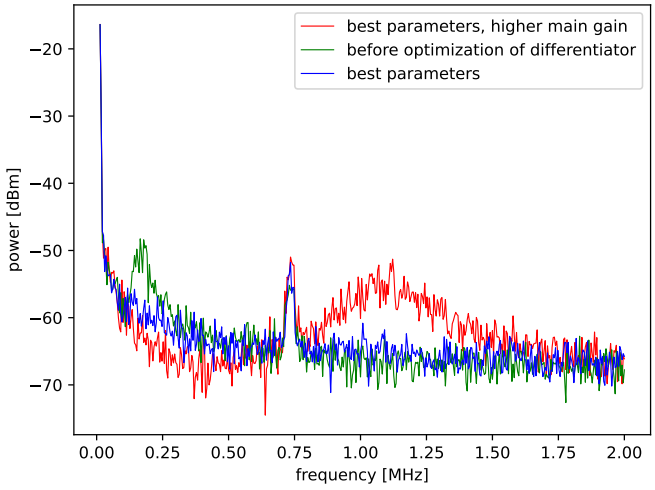

Figure 2.6: Frequency spectrum of error signal for different parameters, the good parameters were the final parameters of the lock

2.3.2 Acousto-optic modulator

Before the control light goes to the optics setup for the Rydberg excitation, an AOM (*3080-125* from *Gooch & Housego*) was placed in front of the fiber (see Figure 2.2 for the optic setup), analogous to the setup in section 2.2 for the probe light. About 90 % of the light before the AOM in transmitted into

the first order.
Using the same method as in section 2.2, the rise and fall time and the beam diameter of the control beam were determined.
The calculated values can be seen in Table 2.2. These values are also sufficiently low to allow shaping of the control pulses in the experiment.

Table 2.2: Rise time and fall time and beam radius calculated from the fit of the control beam, $t_{90/10}$ is the time within the power rises from 10% to 90% (fall from 90% to 10%)

	$t_{90/10}$ [ns]	beam radius [µm]
fall time measurement	108.0 ± 0.5	353 ± 2
rise time measurement	107.6 ± 0.6	354 ± 2

CHAPTER 3

Arducam MT9J001 for beam characterization

One goal of this thesis is to characterize the optic setup for the excitation and probing of Rydberg atoms. For this, the waist of the probe beam, with $w_0 < 10\,\mu m$, must be characterized. Therfore, one needs to have a tool which can capture the intensity-profile of the laser beam at a resolution of a few micrometer. There are two commonly used techniques for this:
First, the knife edge method [26] which scans the beam profile by moving a sharp edge through the beam. This method was discarded as one can not resolve the whole beam profile. In addition, one would need a very precise piezo driven translation stage to work with such small beams.
The second way is to use a camera. This is a very convenient method to characterize the intensity-profile of a laser beam. One can capture the whole structure of the beam-profile, only limited by the resolution of the sensor of the camera. Furthermore, it is a compact setup and easy to use.
In general, this is a straight forward method. However, the *Arducam* that will be used shows a Bayer pattern in the images which limits the resolution. This becomes a problem when imaging the small probe beam. On the other hand, the camera has great advantages which will be discussed in the first section. There, the Bayer pattern will also be discussed. The second section shows how the adjustable gain settings of the camera were used to eliminate it. The last section will present a software developed for the camera, which makes beam characterization easier and can also be used to align laser beams and optics.

3.1 The camera

The *Arducam MT9J001* was chosen because it had the smallest available pixel pitch at the time of 1.67 µm x 1.67 µm [15]. Moreover it is a monochrome camera which is well suited for monochromatic laser beams.
There is the Bayer pattern on the images. Figure 3.1(c) shows a captured beam profile of a 780 nm laser beam near the focus. Due to the small beam diameter, it is not possible to see if the maximum beam intensity is actually in the center of the beam because of the Bayer pattern. As can be seen in Figure 3.1(a), the pattern under uniform illumination looks similar to a Bayer mask. Figure 3.1(b) shows how the uniformly exposed image should ideally look like.

A Bayer mask is an array of color filters [27]. Normally it looks like in Figure 3.2(a), the array consists of 2x2 blocks where one block consists of two green, one red and one blue color filters. This

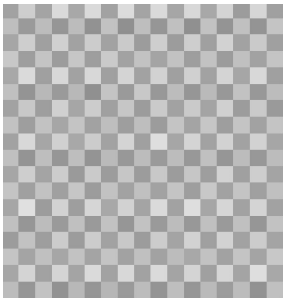

(a) Crop from a uniformly exposed image

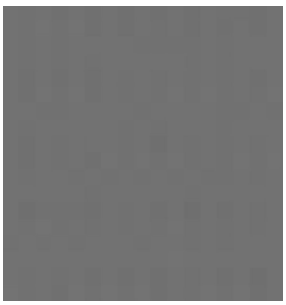

(b)

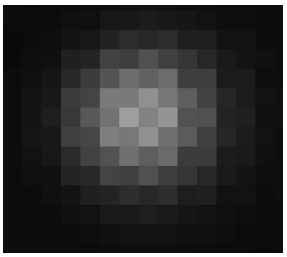

(c) Crop of an image with a 780 nm laser beam near the focus

Figure 3.1: Two sample images showing the Bayer pattern in a) and c). b) shows how the image from a) qualitatively should look without the pattern

way, a color image can be created later by software, in which a 2x2 block is combined to a virtual color pixel.
The filters have a wavelength-dependent transmission, the transmission curves can look e.g. like in Figure 3.3. This means that in a 2x2 pixel block the pixel value depends on the wavelengths. This would look qualitatively like in Figure 3.2(b) to 3.2(d).
Since the pixels do not show different wavelength dependence, it can be concluded that there is no physical color filter on the sensor. This is shown in section 3.2.3. Presumably, the sensitivity of the pixels is calibrated to use the sensor for the color version *MT9J003* [28].

(a) (b) (c) (d)

Figure 3.2: a) shows a typical Bayer mask on a 2x2 Pixel block. Each color corresponds to the wavelength with highest transmission of the filter. b) qualitatively shows the intensity distribution one would observe on a pixel block, illuminated with green light, c) illuminated with blue light d) illuminated with red light

3.2 Calibration

The behavior of the sensor pixels as a function of the intensity of the incident light and the wavelength was measured in the following. This is done to examine how each of the pixels of a 2x2 block have to be calibrated to correct the pattern.
In chapter 4 the beams of a 780 nm and a 480 nm laser are to be characterized. Therefore, the following measurements were also performed with 780 nm and 480 nm laser light.
By using a divergent beam it was ensured that the complete sensor is illuminated uniformly. The

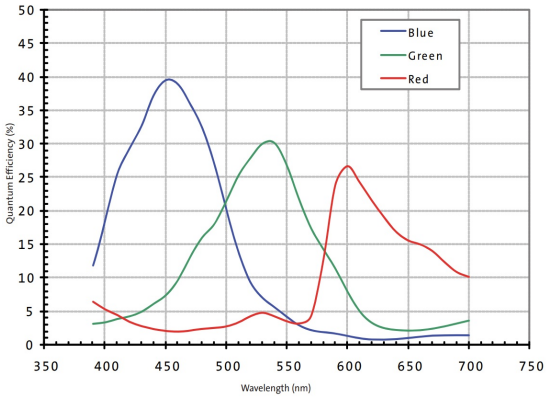

Figure 3.3: Quantum Efficieny Curves of the pixels with blue, the green and the red color filter on the color version *MT9J003* of the *Arducam* [29]

sensor is schematically drawn in Figure 3.4, one can see that each pixel is assigned a coordinate. The coordinates are used in the following to refer to the corresponding pixels.
Since laser light is coherent, interference occurs at the glass plate in front of the sensor, which is visible in the images, such as in Figure 3.5. Therefore, the 40,000 brightest pixels (10,000 pixels for each pixel of the 2x2 block) were used. This was done under the assumption that these pixels are approximately equally illuminated and that the interference pattern is significantly larger than a 2x2 pixel block. With an array size of 2748x3664 pixels, this corresponds to about 0.4 % of the entire sensor.

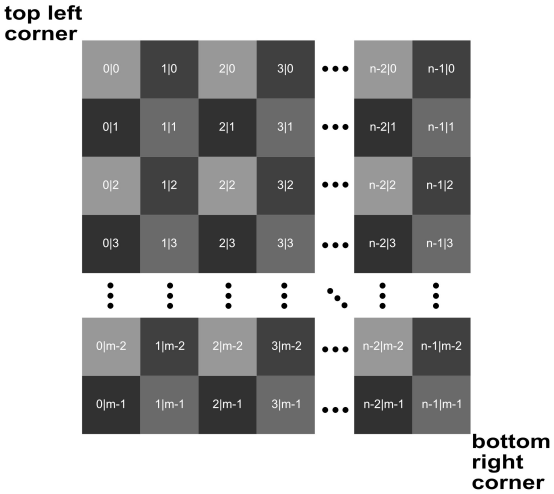

Figure 3.4: Schematic drawing of the camera sensor. Each pixel is assigned a coordinate

The mean values for each of the four pixels from the 2x2 block were then calculated. Although the camera supports 12bit bit depth it was used in 8bit mode. Therefore, the pixel values range from 0 to 255. The 8bit mode was used because the 12bit mode is not supported out of the box by the *Python*

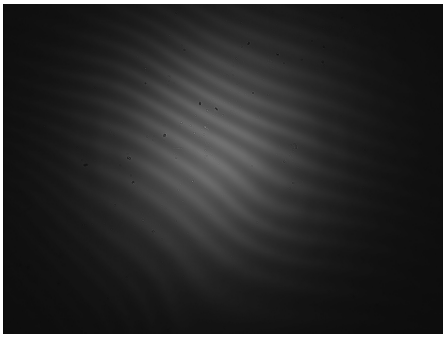

Figure 3.5: Image of a collimated 780 nm laser beam. The interference pattern is caused by the glass plate in front of the sensor

module *Open-CV* [30]. This module is used for image processing and capturing.
Figure 3.6 shows the behavior of all four pixels depending on the beam intensity. It can be seen that the pixel values depend differently on the beam intensity. Furthermore, one can see that all pixels do not behave linearly when the intensity exceeds 50 µW, they saturate. For the measurements of the probe and control beam it is important that the camera is operated in the linear regime.

3.2.1 Customizing the camera gain settings

To remove the pattern, the camera's feature to adjust the gain of the four pixels of the 2x2 block individually is used.
In the following it is explained how the internal gain of the camera works and how the gain settings of a pixel of the 2x2 block can be changed. The block diagram of the camera can be seen in Figure 3.7. The processing of the analog voltage values of the pixel array can be divided into analog signal processing before the ADC (analog-to-digital converter) and digital processing after the ADC. Therefore, there are also two different amplification stages, one analog and one digital [31]. The analog amplification stage amplifies the analog signal of the pixels, in a range of 1x-16x [31] (these are the specifications of the *MT9J003*, but they are the same for the monochromatic version *MT9J001* [28]). This amplification happens before the ADC. The digital gain is applied after the signal has passed the ADC. It ranges from 1x-7x [31].
The analog and digital gain can be adjusted by accessing them over control register. The register addresses for all four pixels are shown in Table 3.1. Each register takes a 16bit value as an input [31]. The first 12 bits are used to adjust the analog gain, the next three bits adjust the digital gain. For a better understanding, this is shown in Figure 3.8. The actual values of analog and digital gain are calculated in the following way [29]:

$$\text{analog gain} = \left(\frac{8}{8 - \text{bit}[9:11]}\right) \cdot (\text{bit}[8] + 1) \cdot (\text{bit}[7] + 1) \cdot \frac{\text{bit}[0:6]}{64} \tag{3.1}$$

$$\text{digital gain} = \text{bit}[12:14] \tag{3.2}$$

Bits 9 to 11 are restricted to a value of 0, 4 or 6 [29]. The first analog gain stage provides the highest resolution. Therefore, this stage will be used in the next section to eliminate the Bayer pattern.
There is a *Python* library from *Arducam*. In it there are two commands with which one can write to

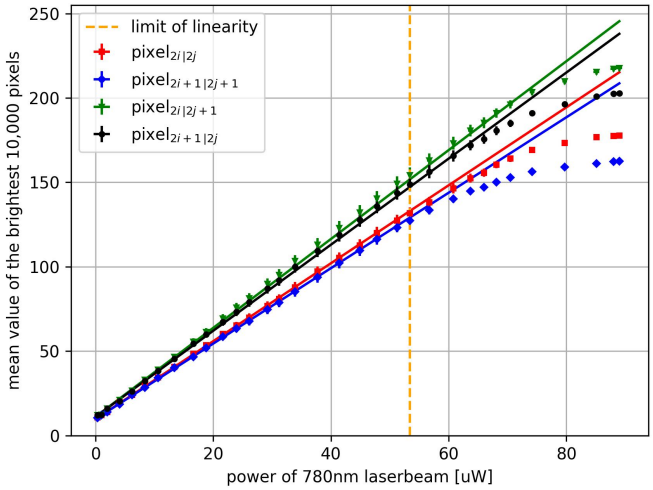

Figure 3.6: Average values of the 10,000 brightest pixels for each pixel of the 2x2 block as a function of the beam intensity. The pixel numbering correspond to Figure 3.4 (pixel error is given by the standard deviation to take possible non-uniform illumination into account)

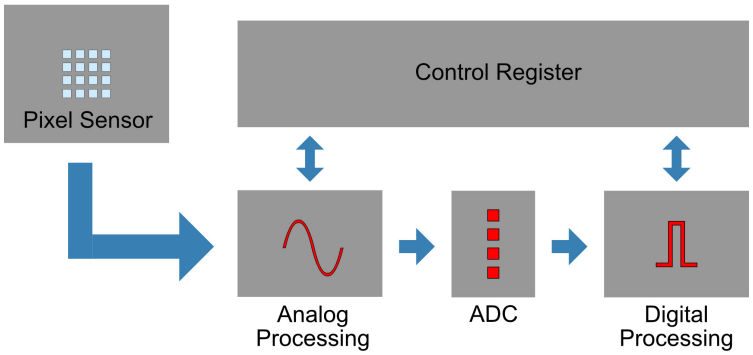

Figure 3.7: Block diagram of camera of the important parts to understand the gain settings, the output of the sensor goes to the analog processing where the analog gain can be adjusted. The data then goes through the ADC. After the ADC, digital processing is applied. Here, the digital gain can be adjusted [31].

the registers and read them out [32]:

```
ArducamSDK.Py_ArduCam_readSensorReg(register_address)
ArducamSDK.Py_ArduCam_writeSensorReg(register_address, value)
```

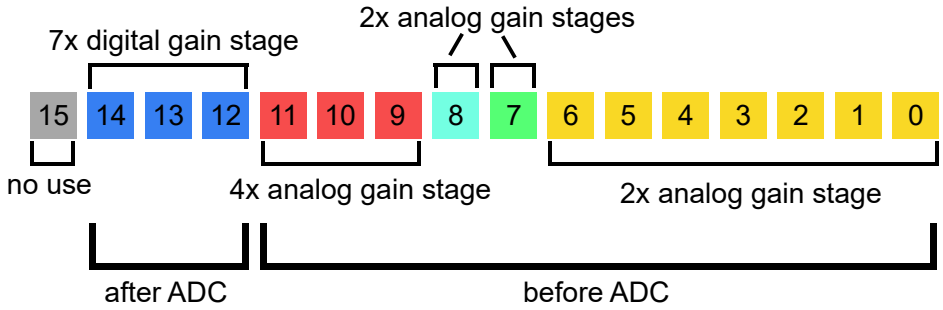

Figure 3.8: Schematic to understand the digital and analog gain stages. The gain register gets 16bit as input value [31]. Bit 0 to bit 11 correspond to analog gain stages, bit 12 to 14 correspond to the digital gain stage

Table 3.1: Register addresses used to change the gain settings [29]

Description	Register address in hex-code	Register address in decimal-code
green1_gain	R0x3056	12374
blue_gain	R0x3058	12376
red_gain	R0x305A	12378
green2_gain	R0x305C	12380

3.2.2 Calibration for 780 nm light

The 780 nm probe laser was used for calibration. It was ensured that the beam diameter at the camera location is large enough to illuminate the entire sensor as homogeneously as possible. In addition, the illumination should remain the same during calibration. Next, care was taken to ensure that the sensor was in the linear range and not saturated. The linearity limit can be taken from Figure 3.6. For this, the mean values were calculated with the same settings as in Figure 3.6 while the camera was running. Then, the brightest pixel was used as reference. The goal was now to bring the average values of the other three pixels to the level of the reference pixel. The procedure can be seen in Figure 3.9. This process was automated in Python.
After each image, the mean values of the three pixels were compared with the reference pixel. Afterwards the first analog gain stages of the pixels were adjusted (increased in this case). After each adjustment, the mean values of the pixels were calculated again and compared with the reference. This was done until the deviation between all pixels and the reference was minimized. Here one is limited

by the discrete values of the gain.
The result of the calibration can bee seen in Figure 3.10. The comparison of this result to Figure 3.6 shows that the calibration process worked. Figure 3.11 demonstrates the difference between an image of a small laser beam taken before and after the calibration. The camera can now be used for characterization of laser beams.

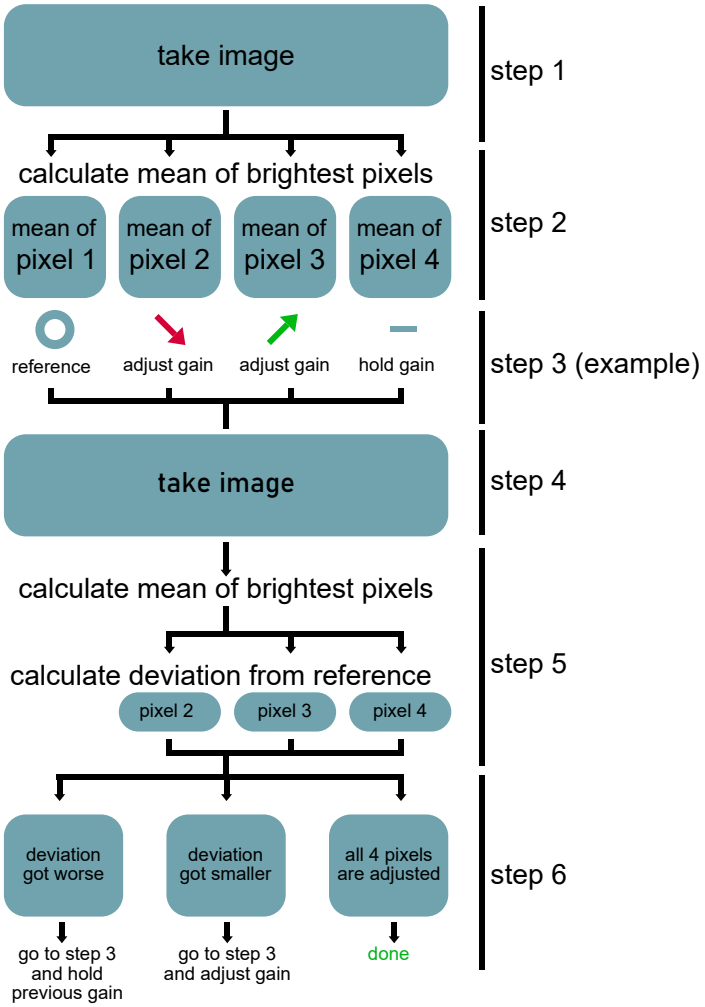

Figure 3.9: Block diagram of calibration process. This process was automated in Python. Here, pixel 1 is used as the reference pixel. The three other pixels should get brought up to the value of the refernce pixel

3.2.3 Calibration for 480 nm light and conclusion

For the characterization of the control beam for the Rydberg excitation, the camera must also work at 480 nm. Therefore, the calibration at 480 nm will be briefly discussed in the following.
If the camera sensor really had a physical Bayer mask, the four pixels at 480 nm would have to behave significantly differently than at 780 nm. In particular, the pixels with a blue color filter should be significantly more sensitive than the others.

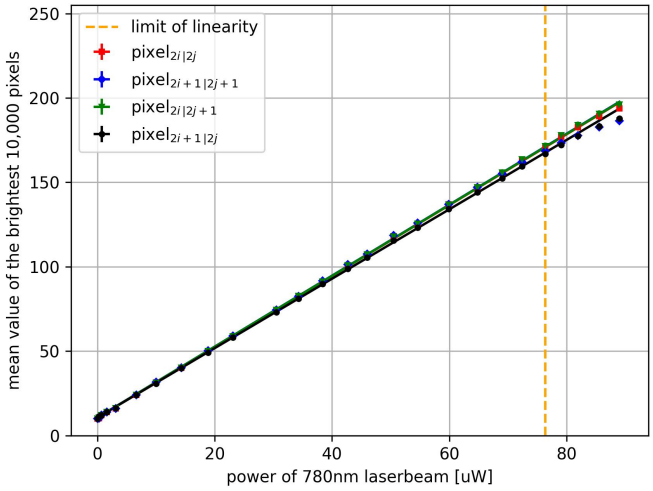

Figure 3.10: Average values of the 10,000 brightest pixels of the 2x2 block as a function of the beam intensity at 780 nm. The pixel numbering correspond to Figure 3.4. This measurement was done after the calibration process. All four pixels are now behaving in the same way.

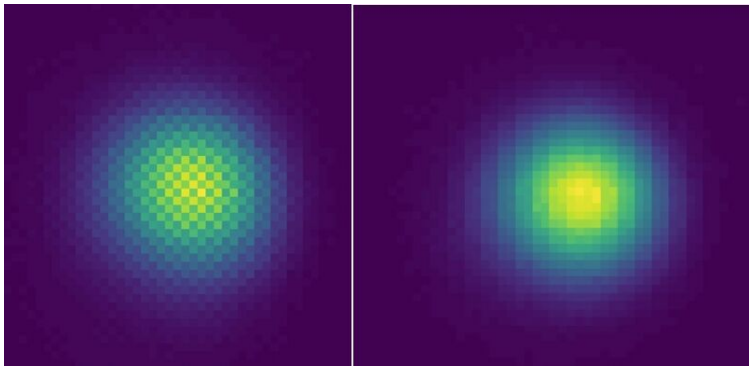

Figure 3.11: Beam profile of a 780 nm before and after the calibration. The Bayer pattern has been eliminated

Without the color filter, the behavior of the four pixels of the 2x2 block at 480 nm should not differ much.
Analogous to section 3.2.2, a series of measurements was made at different beam intensities at 480 nm. The result of the series of measurements can be seen in Figure 3.12.[1]
One can see that the behavior of the pixels relative to each other is not significantly different from the behavior at 780 nm.[2] From this it can be concluded that the camera actually has no physical Bayer mask. Furthermore, the gain settings from section 3.2.2 can be kept. The gain settings from table 3.2 are the final settings used for later measurements at 480 nm and 780 nm. They were also tested by Christoph Biesek (RQO) with another *Arducam MT9J001* and they worked.

Table 3.2: final settings of digital gain that are used for measurements of the probe and the control beam.

gain register in decimal code	gain value in decimal code
12374	4162
12376	4176
12378	4173
12380	4161

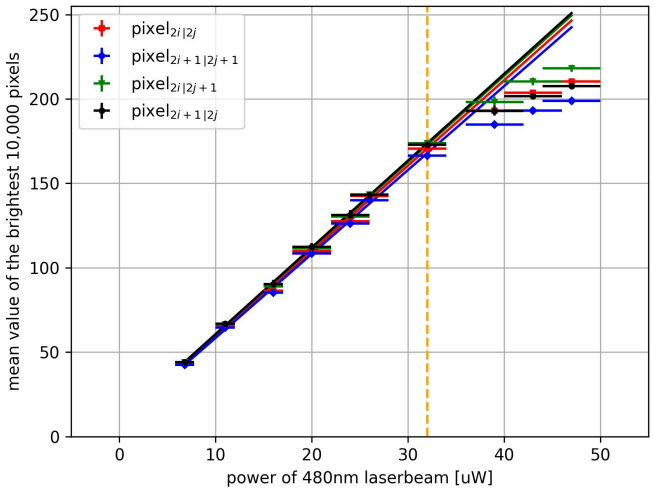

Figure 3.12: Average values of the 10,000 brightest pixels of the 2x2 block as a function of the beam intensity at 480 nm. The pixel numbering correspond to Figure 3.4. The gain settings from the calibration at 780 nm are used in this plot. The calibration also works at 480 nm. High uncertainties of the beam power are a result of fluctuations of the powermeter

[1] The beam diamter at the sensor was larger that at 780 nm because of the higher sensitvity of the sensor at 480 nm (about 10x as large as at 780 nm [33]) at 480 nm.

[2] There is a slightly bigger divergence that in Figure 3.11 which is caused of the higher sensitivity at 480 nm. But this calibration is by far good enough for our purpose.

3.3 Software for beam-profiling and alignment

As discussed in chapter 4, the overlap of the probe and control beams and their waists inside the science chamber is critical for the success of the experiment. To calibrate the setup outside the science chamber, the precision of irises and power meter measurements were not precise enough. Therefore, during the assembly a software was developed (in Python), with which this problem was solved. The functions are briefly presented here.

Functions for alignment of laser beams and optic parts

In the program there is the possibility to use either an existing image or the current image of the camera as a reference. The reference image can then be superimposed with the live image of the camera.[3] Additionally, the summed intensity profiles are plotted in the image.
Figure 3.13 shows the program while aligning a lens. The reference image was set before placing the lens in the beam. In the software, the intensity profiles of the reference image and the live image are displayed. The lens was aligned by matching both profiles.

Figure 3.13: The software for the Arducam is connected to the camera and running on the laptop. The software shows the live image and the intensity profiles of it and overlaps it with a reference images. This picture was taken during the alignment of the lens on the right side.

Functions for beam-profiling

When recording very small laser beams, they only cover a very small part of the sensor. To assess the quality of the laser beam live, the software can automatically zoom in so that the laser beam sits in the center of the displayed image. This is demonstrated in Figure 3.14. Furthermore, pixels that are already saturating (taken from section 3.2.2) are marked red, optimally exposed pixels are marked green. This is an easy way to ensure good exposure when taking an image (see Figure 3.15 as an example).
See the appendix A.3.2 for details on how to get and run the code.

[3] If one uses an existing image as a reference, on has to make sure that the orientation of the reference image and the live camera image is the same.

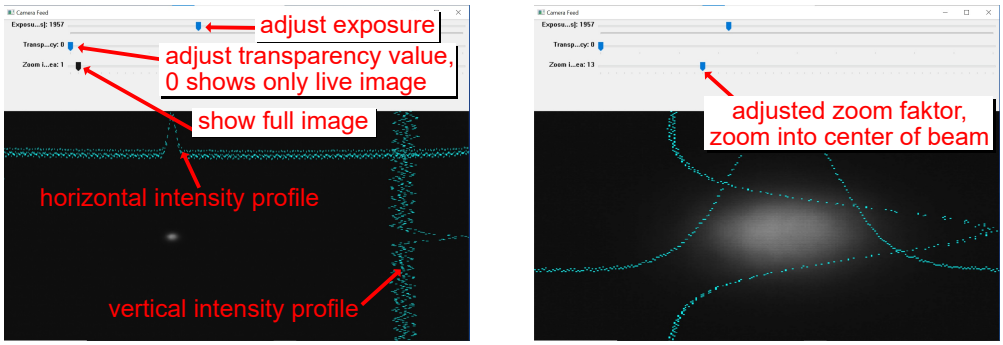

(a) (b)

Figure 3.14: a) shows the functionalities of the software b) shows the activated zoom mode for beam profiling. The beam in b) is the same as in a)

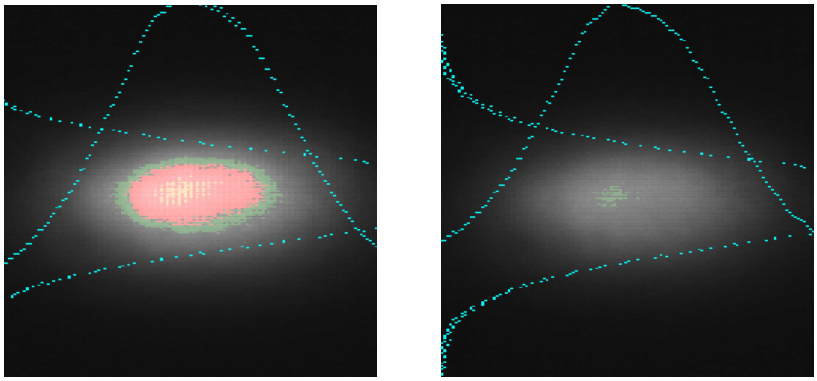

(a) (b)

Figure 3.15: a) shows an overexposed image. The overexposed pixels are painted in red, they are not behaving linearly anymore. b) shows an image with good exposure, pixels that are bright but not saturating are marked in green

CHAPTER 4

Optic setup for excitation of Rydberg atoms in 1D-geometry

In this chapter, the optics setup for the Rydberg excitation is discussed. First it will be explained how the setup is designed and what are the requirements to realize such a one dimensional geometry.
The most important properties of Gaussian beams are summarized.
Subsequently, a test setup is built because one can not characterize the quality of the beam profiles around the focus after the assembly around the science chamber.

4.1 Gaussian beams

A laser beam coming out of a single mode fiber is well described by the Gaussian fundamental mode TEM_{00}. This mode is the fundamental solution of the paraxial Helmholtz equation.
Here, the most important properties of a Gaussian beam are briefly summarized [16].

The distribution of intensity of a Gaussian beam along the axis of propagation z and the radial axis r is given by

$$I(r,z) = I_0 \cdot \left(\frac{w_0}{w(z)}\right)^2 \cdot \exp\left(\frac{-2r^2}{w(z)^2}\right) \tag{4.1}$$

where I_0 is the maximum intensity, $w(z)$ is the radius of the beam in which the intensity falls of to $1/e^2$ and w_0 is the (minimal) radius of the beam at the waist.
The beam radius along the z-axis is given by:

$$w(z) = w_0 \cdot \sqrt{1 + \left(\frac{z}{z_R}\right)^2} \tag{4.2}$$

where

$$z_R = \frac{\pi w_0^2 n}{\lambda} \tag{4.3}$$

is called the Rayleigh range. At $\pm z_R$ the beam has a waist of $\sqrt{2}w_0$. In the focus, the wave fronts are flat, at $\pm z_R$ the curvature is at maximum. The wavelength of the laser is given by λ and n is the

refractive index. The setup is built in free space, therefore $n = 1$ will be used in the following.
Far away from the Rayleigh range, $w(z)$ increases linearly, the divergence of the beam can be described by the angle θ between $w(z)$ and the z-axis. This angle is given by (in paraxial approximation):

$$\theta = \frac{\lambda}{\pi w_0} \tag{4.4}$$

The new radius at the waist w_0^n after a beam propagates through a thin lens can be described by[34]:

$$m = \frac{w_0^n}{w_0} = \frac{1}{\sqrt{\left(1 - \frac{s}{f}\right)^2 + \left(\frac{z_R}{f}\right)^2}} \tag{4.5}$$

where s is the distance between lens and w_0, f is the focal length of the lens and m is the magnification.
It can be seen from (4.3) and (4.4) that a tightly focused beam (small w_0) has a small Rayleigh range and a high divergence. A well collimated beam with a large Rayleigh range implies a large beam diameter. This becomes important in section 4.2 when selecting lenses.
When looking at equation (4.5), one can also see that in order to get a small beam waist one should try to use a big and well collimated input beam (this means big Rayleigh range z_R) and a lens with a small focal length.

4.2 Requirements for the setup

In the introduction 1, the setup for the Rydberg excitation was already introduced. Next, it will be explained in more detail what the requirements are for the setup and how the optics used were selected accordingly.
Figure 4.1 shows a sketch of the planned setup of the atom chip with the oscillator and the probe beam. The possible dimensions of the probe beam are constrained. First, the waist must be small enough to achieve a 1D geometry due to the Rydberg blockade effect, i. e. $w_0 \lesssim 10\,\mu m$ [10].
At the same time, the waist must not be too small, otherwise part of the beam will be cut off by the mechanical oscillator due to the strong divergence of the beam. Figure 4.2 shows the projection of the beam profile for $w_0 = 5\,\mu m$ and $w_0 = 8\,\mu m$ together with the expected dimensions of the oscillator. One can see that at a waist of $w_0 = 5\,\mu m$ the divergence of the beam is already too large.
Furthermore, the focal length of the focusing lens must not be too small (50 mm is already too small), because the lenses are placed outside the science chamber. Figure 4.3 shows a sketch of the chamber. The dimensions are constrained by the Radiation shields. The opposite sides have a distance of 106 mm from the outside.
The control beam should be of such dimension that it covers the probe beam in the z-range which is used for Rydberg excitation (100 µm - 200 µm). The beam radius around the focus should also be large enough such that it provides approximately uniform intensity in the region of the probe beam.
Table 4.1 shows the expected waists at the focus of the probe beam for different combinations of collimator, which is used to collimate the beam coming out of the fiber, and lens, which will focus the beam into the science chamber. Finally, it was decided to use a collimator with a focal length of $f = 25.08\,mm$ and an achromat with a focal length of $f = 80\,mm$. With this one expects a waist of $w_0 = 7.98\,\mu m$. This beam meets the above conditions. Furthermore, the focal length of the lens,

for focusing the beam, is large enough so that the science chamber fits between the lens pair (pair to re-collimate the beam after it passed through the science chamber). An achromat is used because one expects less lens abberations at the focus than with a plano convex lens while being less sensitive to alignment than with an aspherical lens. In addition, it reduces the dispersion of the lens, i.e. for the blue control beam the focal length does not change much.
Table 4.2 shows the expected waist for different lenses of the collimator for the control beam. For this setup a collimator with a lens with focal length of $f = 11$ mm is used (the collimator of the control beam may be replaced later on).
In Figure 4.4 one can see the theoretical projection of the overlap of probe and control beam.

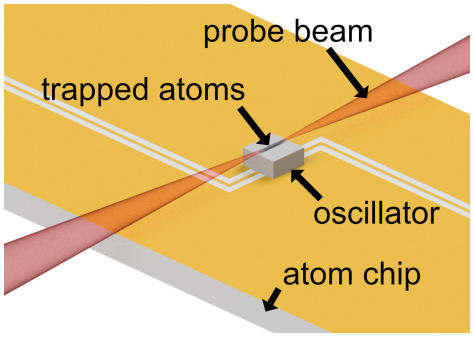

Figure 4.1: Sketch of the atom chip and the oscillator. Atoms are trapped above the oscillator. The probe beam is for the excitation of the Rydberg atoms. The control beam is not included in this picture but will be there in the experiment. Courtesy of Hannes Busche

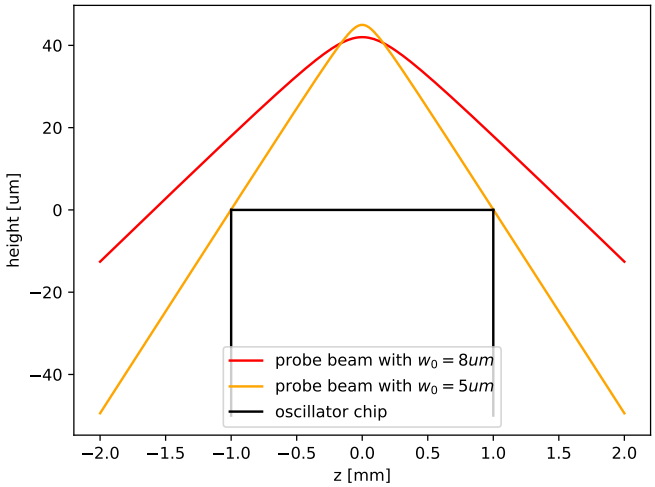

Figure 4.2: Projection of two different beam radius w_0 at focus for the probe beam, the black drawing shows the expected dimensions of the oscillator, the beam with $w_0 = 5\,\mu$m cuts the oscillator

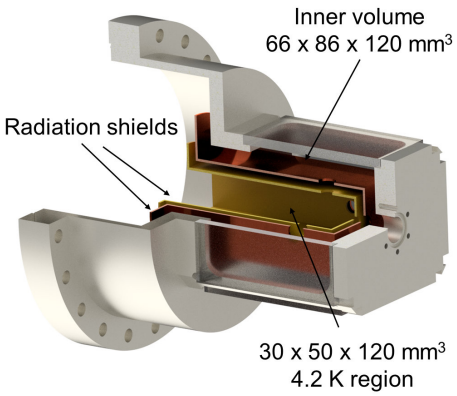

Figure 4.3: Sketch of the science chamber, the dimensions are constrained by the Radiation shields. Courtesy of Cedric Wind

Table 4.1: Expected radius at focus of probe beam for different collimators and achromats, the radius at the focus is given in micrometers, calculations were done by Hannes Busche

collimator	$f = 50\,\text{mm}$	$f = 60\,\text{mm}$	$f = 75\,\text{mm}$	$f = 80\,\text{mm}$	$f = 90\,\text{mm}$	$f = 100\,\text{mm}$
$f = 25.08\,\text{mm}$	4.98	5.98	7.48	7.98	8.98	9.97
$f = 18.09\,\text{mm}$	6.91	8.29	10.36	11.06	12.44	13.82
$f = 12.19\,\text{mm}$	10.25	12.30	15.37	16.40	18.45	20.50

Table 4.2: Expected radius at focus of control beam for different outcoupler lenses, the waist is given in micrometers, calculations were done by Hannes Busche

collimator	$w_0[\mu\text{m}]$
$f = 4.51\,\text{mm}$	30.23
$f = 6.24\,\text{mm}$	22.29
$f = 8.0\,\text{mm}$	17.46
$f = 11.0\,\text{mm}$	12.72

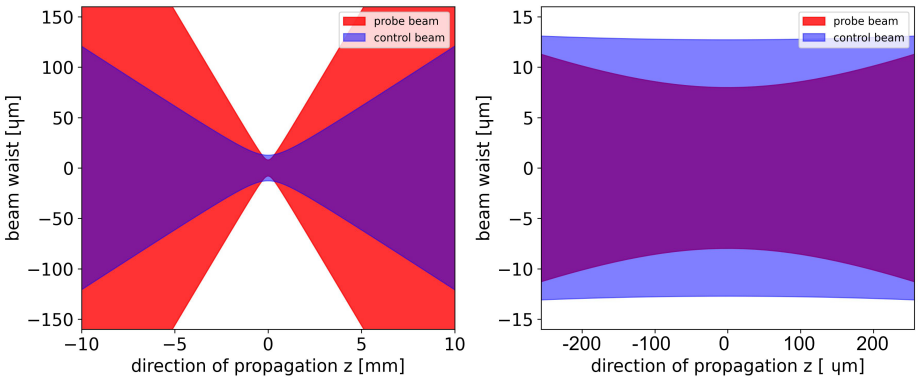

Figure 4.4: Projection of theoretically expected probe beam and control around the focus, left picture shows the dimensions of both beams over a distance along the optical axis of 20 mm, the right picture shows the dimensions inside the Rayleigh range in both directions of the probe beam

4.3 Design

The Figure 4.5 shows the planed setup including all additionally required optics. In table 4.3, all used optics are listed together with a short description.

4.3.1 Probe beam

As one can see, the setup for the probe beam is symmetric, this way, one can use probe light from both direction while the foci of both beam should match.
The first step is the collimation of the fiber coupled probe light with the 25.08 mm collimator. Next, the beam splitter on both sides are there to get a second arm to collect the probe light. From there, the probe light will go to to single photon counters. The beam splitters are for the probe light coming from the opposite site (left arm will fiber couple the probe light coming from the right collimator and vice versa). The telescopes are there to provide the highest coupling efficiency into the fiber (the dimensions of the telescopes and the collimator are based on measurements of coupling efficiency, which are explained in more detail in section 4.4.1).
The next import optics are the two 80mm achromats which are used to focus the probe beam, as well as the control beam. The science chamber will sit between the two lenses, in Figure 4.5 the chamber is represented by the glass plates. Furthermore, there are pairs of two waveplates, one $\lambda/4$ and one $\lambda/2$ waveplate, on both sides of the setup. These are there to control the polarisation of the probe light.

4.3.2 Control beam

The fiber guided control beam gets collimated by the 11mm collimator.
After that, there is also a pair of waveplates to control the polarisation.
The next important part is the dichroic mirror which has a cut off wavelength of 650 nm. This way the mirror acts as such for the control beam while the probe beam gets transmitted.
The pair of the two achromats should then focus the control beam at the same position as the probe beam.
On the other side, there is another dichroic mirror of the same type, this is necessary to collect the control light again with a photodiode.

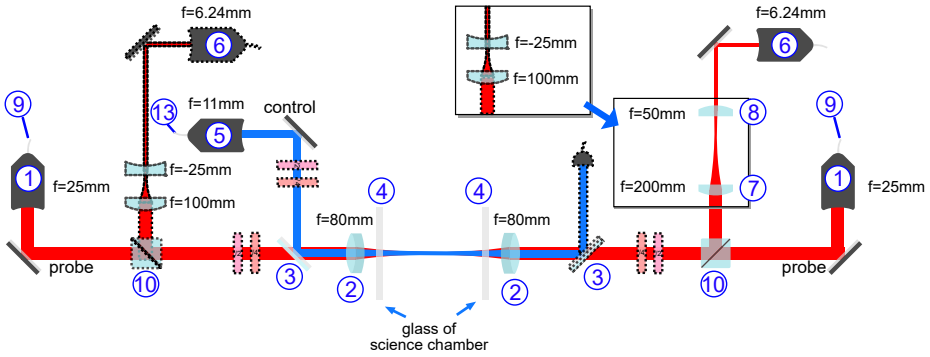

Figure 4.5: Planned setup, the probe beam is shown in red while the control beam is shown in blue. The optics outlined in dashed lines were not installed during this thesis, the telescope on the right will be replaced by the telescope which is outlined in dashed lines. The numbers correspond to the items in Table 4.3

Table 4.3: Used optic parts for probe/control-setup. The numbers corresponds to the numbers in Figure 4.5

number	item	description
1	Thorlabs TC25APC-780	triplet collimator for fiber coupling of probe beam
2	Edmund Optics #49-331	achromat with $f = 80\,\text{mm}$
3	Thorlabs DMLP650	dichroic mirror with cut off wavelength of 650 nm
4	Edmund Optics #34-430	plate of same glass (NKB7) and thickness (6 mm) as science chamber
5	Thorlabs A220TM-A	aspheric lens, $f = 11\,\text{mm}$, for fiber coupling of control beam
6	Thorlabs A110TM-B	aspheric lens, $f = 6.24\,\text{mm}$, for fiber coupling of probe beam to SPCMs
7	Thorlabs LA1708-B	apsheric lens, $f = 200\,\text{mm}$, for telescope of separate arm
8	Thorlabs LA1131-B	apsheric lens, $f = 50\,\text{mm}$, for telescope of separate arm
9	Thorlabs P3-780PM-FC-10	single mode fiber for probe beam
10	Thorlabs PBS12-780	Polarizing Beam Splitter to sperate probe arms
11	Union Optic WPZ2312-780-M25.4	half waveplate
12	Union Optic WPZ4312-780-M25.4	quarter waveplate
13	OZ Optics QPMJ-3AF3AF-488-3.5/125-3A-8-1	single mode fiber for control beam

4.4 Assembly of the setup

In the following, the construction of a test setup is discussed. Furthermore, the alignment techniques are presented, which are very crucial for good beam quality at the focus as well as a high efficiency for the fiber coupling of the probe light.
In addition, to check the beam profiles of both beams, the camera from chapter 3 is used to record images of the beam around the focus along the optical axis. Also, the influence of the optical parts on the beams are discussed.

4.4.1 Probe-beam

This section will cover the setup of the probe beam.

Outcoupling of the probe beam from a pm single mode fiber

The first step was to collimate the probe light from the polarization maintaining single-mode fiber. For outcoupling, the triplet collimator from table 4.3 is used because it promises a high beam quality. The diameter, divergence and ellipticity of the beam depends on the fiber used (it also depends on which end of the fiber is screwed into the collimator). When the fiber is screwed into the holder of the collimator, the fiber end does not sit in exactly the same position for all fibers due to production tolerances. A deviation from the intended position results in convergence or divergence of the beam behind the collimator. Furthermore, there is also a production tolerance on the mode field diameter at the output of the fiber.
Hence, one wants to select the fiber that produces the best beam profile that is closest to the theoretically expected profile and also shows no defects in the beam profile. Therefore, two different types of fibers were tested (seven different fibers were tested in total for both directions) by measuring the beam profile after the collimator.[1]
The first type is the *PMJ-3AF3AF-850-5/125-3A-8-1* fiber from *OZ Optics* which has a smooth, angular

[1] For this purpose, images of the beam were taken at different distances. For this as well as for all other camera measurements, a background measurement without laser beam was always subtracted. This way the gaussian fits reproduce the beam profile way better.

polished end. The second typ is the *P3-780PM-FC-10* PM singlemode fiber from *Thorlabs* which has a round polished end. Figure 4.6 shows the horizontal and vertical radius of the beam along the optical axis for three different fibers, one fiber from *OZ Optics* and two from *Thorlabs*. With the single mode fiber from *OZ Optics* one sees a rather large deviation between horizontal and vertical waist of about 4.5 %. The assumption is that the fiber is not centered on the optical axis of the collimator because of the angled polished end.
For the first single mode fiber from *Thorlabs* one can see that the difference between vertical and horizontal beam radius has disappeared, but the beam shows a clearly visible convergence, the beam is not as well collimated as it would be expected (at $z = 0.2$ m the beam is about 16 % smaller than expected). This is the effect of the production tolerance of the position of the fiber.
The second fiber from *Thorlabs* produces a better collimated beam which has a bigger radius (about 6 % smaller than expected) and also has a smaller ellipticity (difference of the two axis of about 2 %). Therefore, the second fiber was used for the setup.
With the beam profile after the collimator one can give a rough estimation of the expected dimensions at the focus after passing the 80mm achromat:

$$w_0^{\text{vertical}} \approx 8.4\,\mu\text{m} \tag{4.6}$$

$$w_0^{\text{horizontal}} \approx 8.5\,\mu\text{m} \tag{4.7}$$

These values fall within the error bar given by the production tolerance on the mode field diameter.

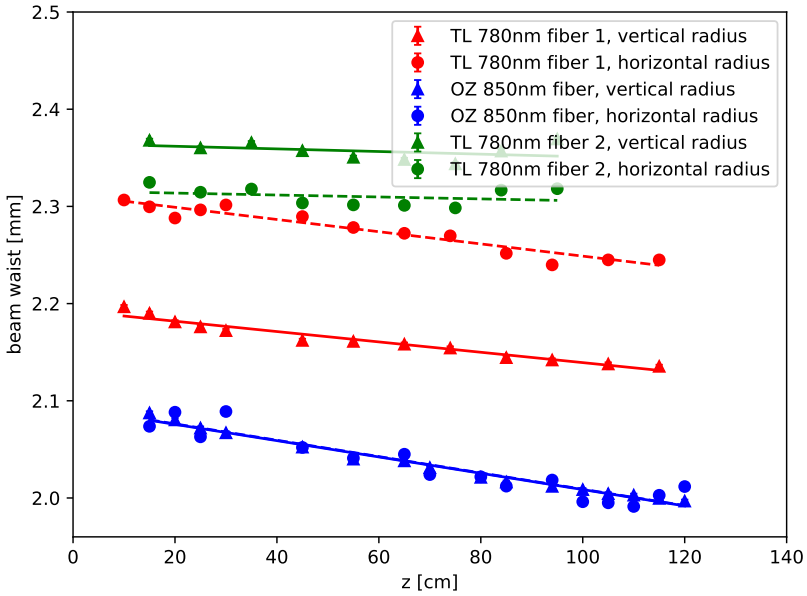

Figure 4.6: Vertical and horizontal radius along the optical axis of three different fibers are shwon. Error bars are too small to be seen. Systematic errors are caused by changes in the interference pattern when moving the camera

Probe beam after Achromat EO #49-331 , f= 80 mm

Next, the achromat from table 4.3 is placed in the optical path. Here, the alignment is discussed in more detail, because the lens has to be placed very precisely to avoid distortion and abberation. Then, the beam is measured around the focus.
In the ideal case the beam passes the lens orthogonally and exactly in the center.
To realize this, the first important point is that the lens sits in a height-adjustable mount, since even the smallest spacer disc (which where available in the lab) with a diameter of 75 µm [35] have already led to a clearly visible beam offset.
Furthermore, the beam that exits the collimator should already be very well aligned (with the camera).
For aligning the lens, a 2f setup was chosen. One can see the setup in Figure 4.7. This means, that the camera is positioned at a distance of two times the focal length from the lens. At this position, the beam (after passing through the lens) should be a mirror image of the beam that is not passing through the lens. This way one can align the lens by matching the position of the beams, with and without the lens, on the camera sensor. Furthermore, one can spot assymetries in the beam with this technique. This was done with the software from 3.3.
It turned out that this technique is more precise than using two apertures and a powermeter to place the lens (for example, you can already see a very clear offset of the beam, depending on how tightly the screw for mounting is tightened).
Figure 4.8 shows the vertical and horizontal beam profile with and without the lens. Both profiles match very well, especially the horizontal axis.
Next, the beam around the focus was measured. For this purpose the camera was mounted on a micrometer translation stage and moved along the optical axis.[2] In Figure 4.9 one can see some selected images of the beam around the focus. The beam looks Gaussian, there are no obvious aberrations or distortions. At the focus, however, the quality of the beam cannot be judged very well because here one pixel is already 10 % of the expected beam diameter.
Gaussian profiles, according to the exponential part of equation (4.1), were then fitted to the data. For this purpose, the horizontal pixel data was summed up for the vertical axis and vice versa. The radius could then be determined from the Gaussian fits. The function (4.2) was fitted to the determined radii, both for the vertical and the horizontal axis. Figure 4.10 shows the radii depending on the position along the optical axis. From the fit one can extract the radius of the beam at focus:

$$w_0^{\text{vertical}} = (7.965 \pm 0.003)\,\mu\text{m} \tag{4.8}$$

$$w_0^{\text{horizontal}} = (8.384 \pm 0.009)\,\mu\text{m} \tag{4.9}$$

The horizontal waist agrees with the approximated waist from section 4.4.1. The vertical waist is smaller, just as expected but it is closer to the theoretically expected value of 7.98 µm. than the approximated value from 4.4.1.
The horizontal fit agrees very well with the data, also with the data far away from focus. The vertical fit does not suit the radii around the focus and the data far away from the focus at the same time. One factor why the fit further away from the focus does not fit so well could be interference on the glass plate of the camera, which starts to play a role at the size. Figure 4.11 shows an example of a fit further away from focus. Here, one can see that there is an interference-like pattern on the intensity

[2] It was payed attention to prevent any tilting of the camera or the translation stage. Furthermore, it was tried to measure symmetrically around the focus.

profile in the vertical axis. This could be caused by the glass plate of the camera. At the focus it could happen that due to the smaller ratio between pixel size and beam size the result is inaccurate.
Furthermore, the fit depends on how many images are taken at which distance, this dependence is bigger than the estimated errors from the fit.
In any case, there are small systematic errors due to the measurement with the camera. The determined value of w_0 is more trustworthy for the horizontal axis than for the vertical axis.
One can also see from Figure 4.10(b) that there is a small astigmatism, but it is very small compared to the Rayleigh Range (a quantitative analysis will follow later) and therefore not relevant for the experiment.

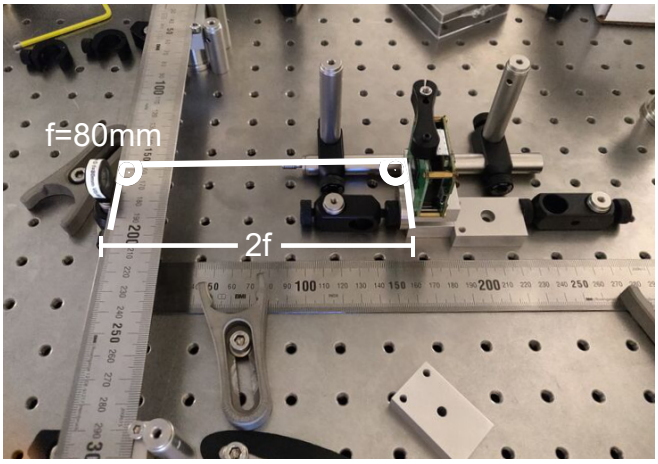

Figure 4.7: 2f setup for lens alignment with camera, the ruler holds the lens at same distance to camera and prevents tiltting of the lens

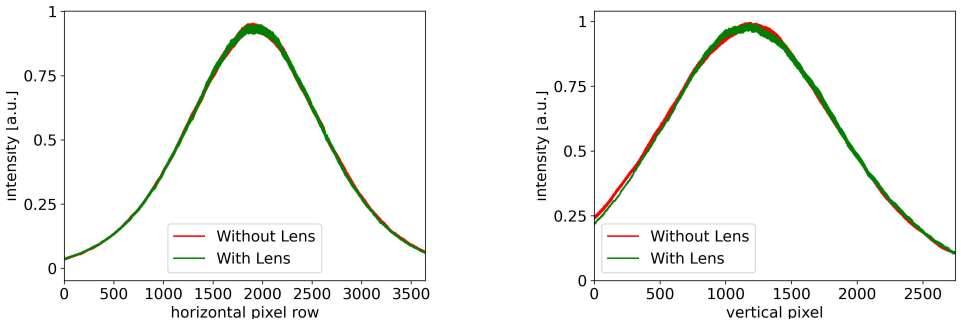

(a) Horizontal beam profile

(b) Vertical beam profile

Figure 4.8: Beam profile of probe beam with and without lens, camera was positioned at 2f distance from the lens position

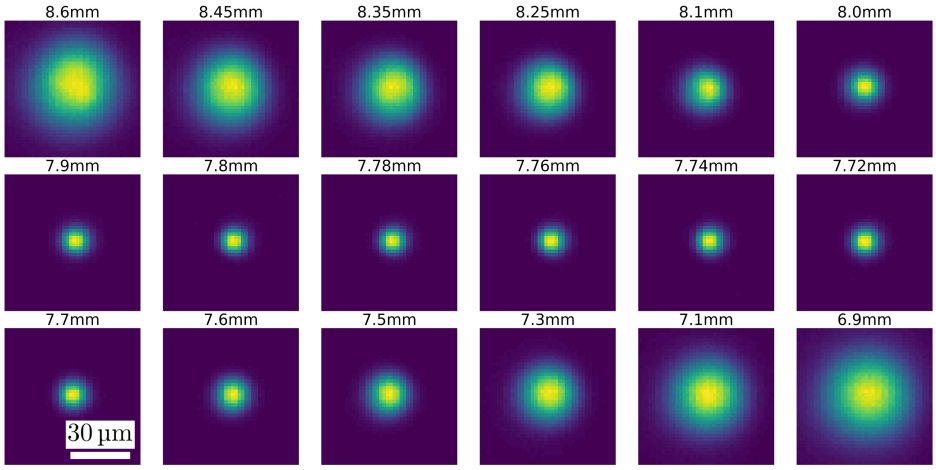

Figure 4.9: Probe beam at different points along the direction of propagation around the focus. the position above the pictures is the position of the translation on its scale along the optical axis.

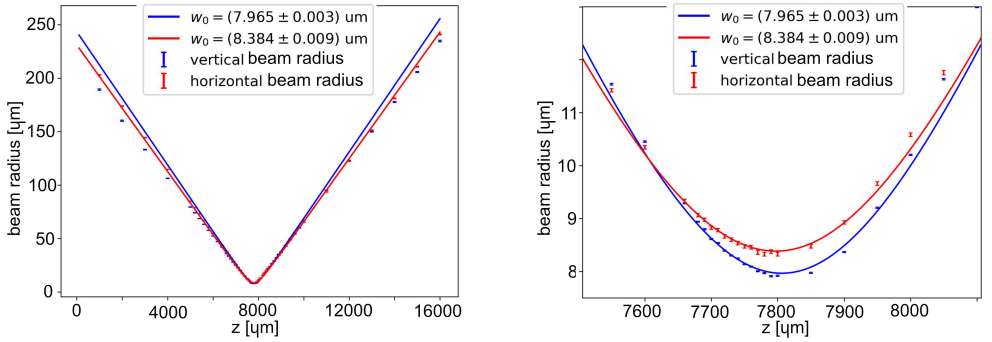

(a) Plot shows all measured data

(b) Plot shows a zoom into the Rayleigh range

Figure 4.10: Gaussian beam waist fit after first lens for vertical and horizontal axis

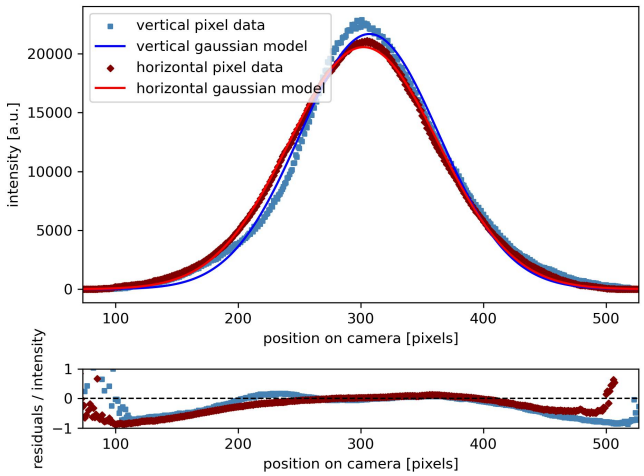

Figure 4.11: Gaussian Fits of probe beam after the first lens further away from focus

Probe beam with dichroic mirror

For the control beam to be able to overlap with the probe beam later, the dichroic mirror was placed in the beam path next.
The mirror has a cut off wavelength of 650 nm, i.e. the 480 nm control light is reflected, the 780 nm probe light is transmitted. Ideally, one expects only a beam offset in the horizontal plane due to the mirror, the height of the beam should remain the same. In fact, one also saw a small beam offset in the height, which means that the mirror surface is not perfectly orthogonal to the beam. It turned out to be much easier to first place the mirror in the beam path and then realign the lens. Subsequently, the beam was measured again around the focus with the camera. Figure 4.12 shows five selected images of the beam. Then, the function (4.2) was fitted to the determined radii. The fit is shown in Figure 4.13. From the fit, the following values are extracted for the vertical and the horizontal axis.[3]

$$w_0^{\text{vertical}} = (7.912 \pm 0.002)\,\mu\text{m} \tag{4.10}$$

$$w_0^{\text{horizontal}} = (8.112 \pm 0.003)\,\mu\text{m} \tag{4.11}$$

$$\tag{4.12}$$

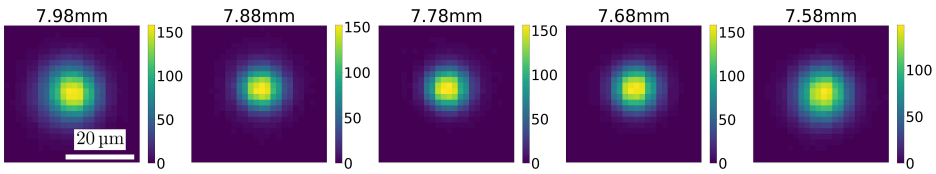

Figure 4.12: Images of the beam around the focus after the first lens and the dichroic mirror in a range of 400 µm, center image is at focus. The position above the pictures is the position of the translation on its scale along the optical axis. The colorbars show the values of the pixels.

imaging of focus with microscope

At the focus, the beam diameter is so small that even the camera cannot resolve smaller details of the beam profile. Therefore, a microscope was used to better resolve the beam within the Rayleigh range. This was necessary to judge the quality of the beam profile at focus. The microscope setup is described in more detail in the appendix in section A.1. With this setup a magnification m of

$$m = 19.8 \pm 0.2 \tag{4.13}$$

was achieved. This was used to measure the beam around the focus again. Two series of measurements were performed with the microscope, one with the camera in the normal position and one with the camera rotated 90 degrees. Thus the horizontal axis can be used for the determination of the radii of both beam axis[4]

[3] The small difference to the values from the previous section could be caused by the fact that more measurements around the focus (also more symmetrically) were taken.

[4] It was noted that the vertical intensity profile on the camera fluctuated slightly. Therefore, several images at the same position were taken near the focus to investigate the effects of the fluctuations. They are taken into account for the

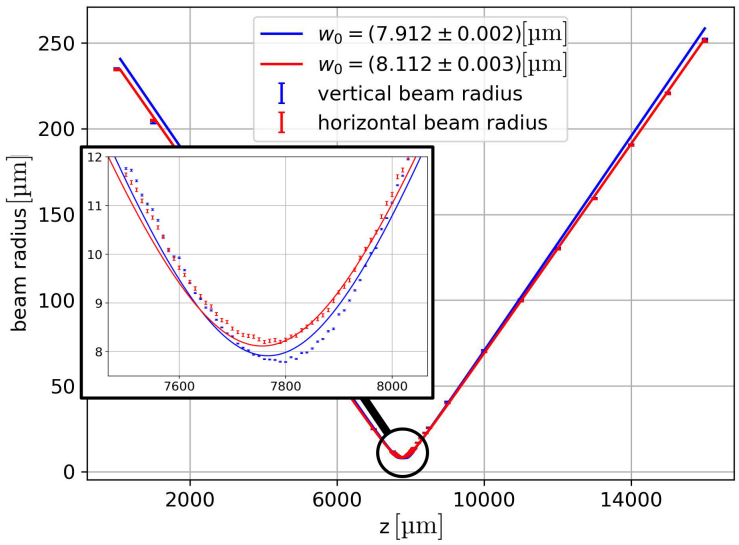

Figure 4.13: Gaussian beam waist fit for vertical and horizontal axis of probe beam after first lens and dichroic mirror

In Figure 4.14 one can see the fits to the data for both series of measurements. Only data within the Rayleigh range was considered, because the setup does not work well outside the Rayleigh range due to the size on the camera sensor, outside the Rayleigh range the interference patterns on the glass plate of the camera also started to distort the measurements.
This results in the following weighted mean values for the radius at focus for both axis (here the magnification factor as well as the uncertainty on the factor was already taken into account):

$$w_0^{\text{vertical}} = (7.56 \pm 0.08)\,\mu\text{m} \tag{4.14}$$

$$w_0^{\text{horizontal}} = (7.69 \pm 0.08)\,\mu\text{m} \tag{4.15}$$

The values deviate 4.7 % percent in the vertical axis and 5.5 % percent in the horizontal axis of the previous measurement, the error bars do not overlap. Since the values are further away from the theoretically expected values, it can be assumed that the magnification of the microscope was overestimated. See the appendix in section A.1 for more details.
Figure 4.15 shows five images in the range of ±100 µm around the focus. The beam looks Gaussian and there are no visible abberations.[5]

From both measurements one gets an offset Δz between the vertical and horizontal focus position which are consistent with each other. This results in an offset of

$$\Delta z = (21 \pm 3)\,\mu\text{m} \tag{4.16}$$

uncertainties of the radii from the Gaussian fits. It could be related to the rolling shutter, the mounting of the microscope or the polarisation of the light.

[5] You can see a slight ellipticity in the diagonal. The ellipticity is an effect of the camera. This is explained in detail in the appendix in section A.3.1.

This corresponds to about 4 % of $2 \cdot z_R \approx 520\,\mu m$. This value is small enough to not matter for the experiment.

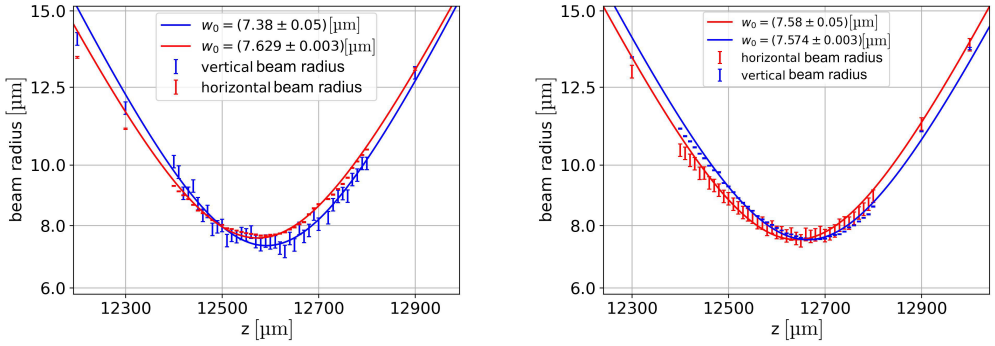

(a) (b)

Figure 4.14: Gaussian beam waist fit after first lens and dichroic mirror, data was taken with the microscope setup, left plot shows the measurement with the camera in normal position, the right plot shows the measurement with the camera turned 90 degrees. The vertical and horizontal radii in the plots are in the lab frame.

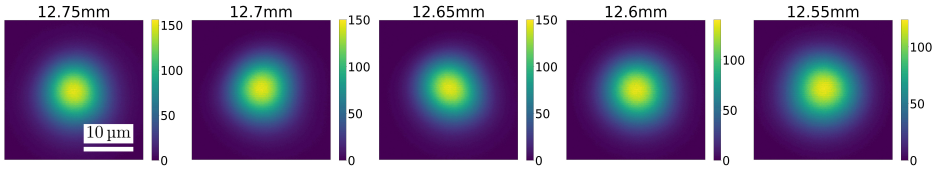

Figure 4.15: Images of the probe beam after the first lens and the dichroic mirror around the focus in a range of 200 µm, center image is at focus, images were taken with the microscope setup. The position above the pictures is the position of the translation on its scale along the optical axis. The colorbars show the values of the pixels.

Probe beam with first glass plate inserted

To simulate the actual setup, a glass plate of the same type as the science chamber glass was placed in the beam path.
Ideally, one would only expect a shift of the focus position. Because of the longer optical path length inside the glass one would expect a shift of the focus position of +2 mm relative to the focus position with no glass. For this calculation, a refractive index of $n = 1.5$ was assumed [36], the glass is *NBK7* of 6 mm thickness.
Because the microscope setup with camera was not moved since the last section, the measurement with the glass plate can be used to calculate the offset of the focus position. To align the glass the beam with glass plate was matched with the beam without the glass pate, this means that the surface of the glass plate is placed orthogonal to the beam. After the alignment, a measurement around the focus was performed with the microscope.
Figure 4.16 shows the fit of the radii in dependence of the position along the optical axis. The radii at the focus agree well with the radii from the measurement from Figure 4.14(b) without glass plate. In comparison with the measurement without the glass plate, there is an offset of the focus further to the

rear of

$$z_{\text{shift}} = (2.03 \pm 0.01)\,\text{mm} \tag{4.17}$$

This agrees well with the expected offset of 2 mm. Figure 4.17 shows images around the focus. There are still no abberations visible.
The second glass plate was then placed in the beam path. Here, care was taken to eliminate beam displacement by the glass plate.

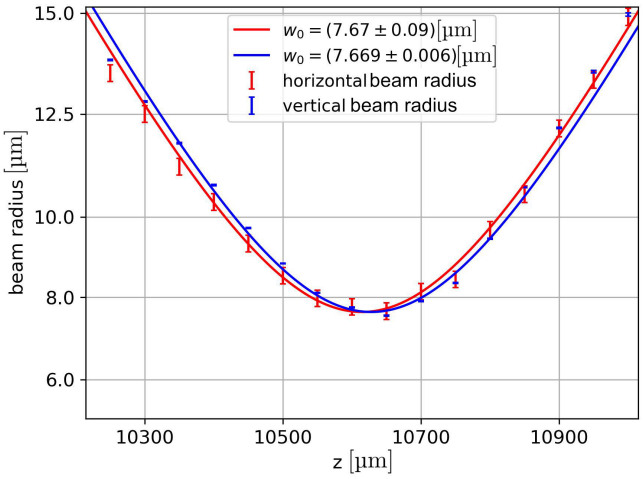

Figure 4.16: Gaussian beam waist fit fit within the Rayleigh Range with first glass plate inserted, camera is turned 90 degree, data was taken with microscope setup

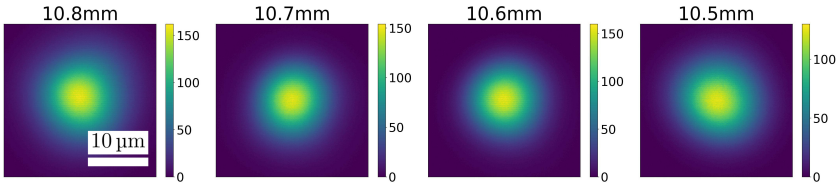

Figure 4.17: Images of the beam around the focus after the first lens and the dichroic mirror and the first glass plate in a range of 300 µm, the images were taken with the microscope setup. The position above the pictures is the position of the translation on its scale along the optical axis. The colorbars show the values of the pixels.

Placement of second lens

Because it is not possible to measure around the focus inside the science chamber, one needs another way to make sure that the position of the foci of the probe beams coming from both directions match. For this purpose, one can take advantage of the fact that Gaussian optics is reversible. This means that it does not matter from which direction the beam comes. Therefore one can assume that the foci match in both beam directions if the coupling efficiency is as high as possible and equals in both beam directions. Therefore, in this section it is discussed how the second lens was placed for collimating the beam and how the coupling into the fiber was optimized.

Since the probe setup is symmetrical, the same lens and collimator are used (see Table 4.3), also the single mode pm fiber is the same. In the theoretical ideal case, both fiber couplers would produce a collimated beam of same dimensions. The second lens would then only have to be placed so that the beam behind it is collimated as well as possible. It was already discovered that this is not the case, the beam profile is already visibly different for different fibers. Therefore the position of the second lens has to be adjusted so that the beam profile after the lens matches the theoretical beam profile which would come out of the second collimator as good as possible.
The idea was now to couple the beam into the fiber in the collimated case first. Then one can vary the position of the lens and at the same time optimize the fiber coupling until one has found the optimal position of the lens. Then one just has to make sure that the lens does not move during mounting. The exact procedure is described in detail in the appendix in section A.2.
This way, a coupling efficiency into the fiber of about 87 % could be achieved. To check that the coupling efficiency is the same for both directions the probe light was send from the opposite direction. The coupling efficiencies have overlapped within the fluctuations of the measurement. Therefore, it can be assumed that both foci are at the same position.

Coupling to single photon counting

Next, the probe beam was fiber-coupled in a second arm. The light will later go to SPCMs. To achieve the highest possible coupling efficiency, the beam profile after the coupling lens must match as closely as possible the beam profile that would theoretically come out of the fiber. Since the degree of freedom to move the lens position was already used to maximize the coupling efficiency into the second triplet collimator, this is not an option for fiber coupling to the SPCMs. Therefore, self-built fiber couplers (with telescope in front) were used here. The coupling efficiency can be maximized by the position of the lens of the fiber coupler.
Three combinations of telescopes and coupling lenses were used. The measured coupling efficiency of the systems is listed in Table 4.4. It can be seen that the 4:1 telescope with a $f = 200\,\text{mm}$ and a $f = 50\,\text{mm}$ lens and a collimator lens with $f = 6.24\,\text{mm}$ has the highest coupling efficiency with about 85 %.[6]

Table 4.4: Fiber coupling efficiency of probe beam into second arm for three different combinations of telescopes and coupling lenses

telescope	collimator lens f [mm]	coupling efficiency [%]
2:1	11	79
4:1	6.24	85
-	25	79

4.4.2 Control-beam

The next step was to overlap the control beam with the probe beam.
The beam was first collimated using the shear plate interferometer [37] from *Thorlabs* [38] and then roughly overlapped with the probe beam using two apertures, one between the glass plates and one

[6] The dimensions of the telescope lenses will be changed for the real setup to save space on the table.

behind. Two things had to be done now. First, the position of the control beam had to be adjusted so that it overlaps as much as possible with the probe beam. Second, the position of the focus of the control beam had to be adjusted such that the foci of the probe and control beam are in the same position. Due to the dispersion of the lens, the foci are slightly apart (when both beams are collimated in front of the lens).
To optimize the position and angle of the control beam, the camera and translation stage were used to compare the control beam and probe beam alternately in front and behind the focus. To adjust the focus of the control beam, the camera was moved with the translation stage to the focus point of the probe beam. Then the position of the lens of the collimator of the control beam was adjusted until the focus point of the control beam was also in the plane of the camera sensor.
Figure 4.18 shows the overlap of probe and control beam. You can see that the control beam has a slight diagonal offset relative to the probe beam of about 4 µm .[7]This can be easily corrected, but was not done due to time constraints.
Figure 4.19 shows the determined radii at the waist (horizontal and vertical) of the control and probe beams. It can be seen that the control has a slight astigmatism which is not a problem for the experiment.[8] Both foci are at the same position. The radii of the control beam are about 2 µm larger than expected, this is due to the shifting of the collimator lens. This is beneficial for the experiment, as the intensity of the blue light in the probe beam region is more uniform.

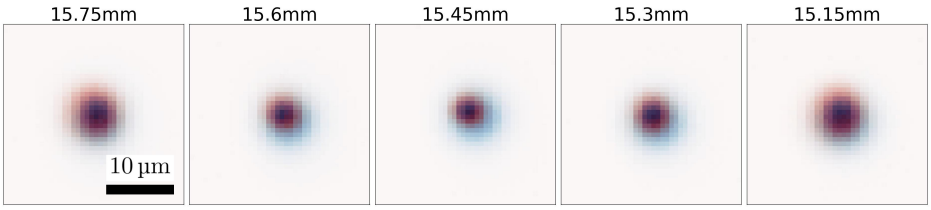

Figure 4.18: overlap of probe images (red) and control images (blue) in a range of 600 µm, background subtracted, middle picture is at focus, the position above the pictures is the position of the translation on its scale along the optical axis

[7] This is due to the fact that the beam position was optimized by aligning it with the probe beam further away from the focus. A small offset of a few micrometers is not easily visible there. This can be solved by looking at the overlap at the focus during the optimization.

[8] The control beam is also asymmetric. Therefore one could think about replacing the collimator of the control beam in the future.

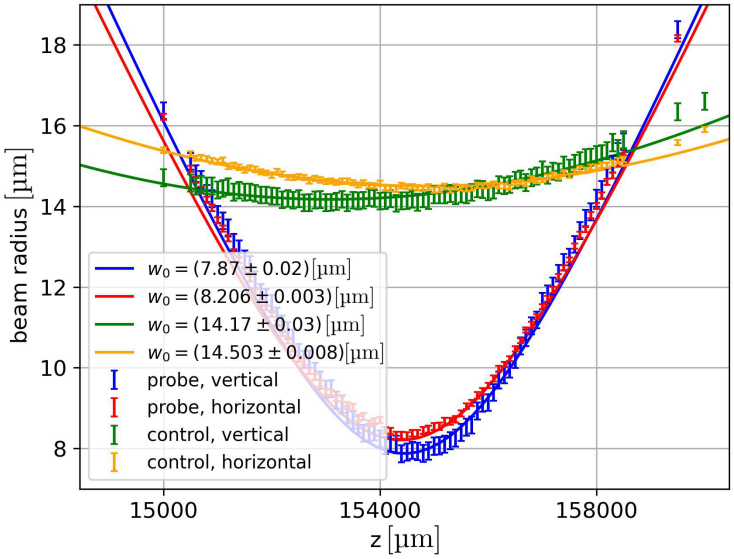

Figure 4.19: Gaussian beam waist fit of probe and control beam for both axis around the focus

CHAPTER 5

Summary and outlook

In this thesis, the laser system and optical setup for Rydberg excitation of ^{87}Rb atoms as part of a hybrid quantum system was designed and characterized.

First, the laser system was set up and characterized. It consists of a 780 nm probe laser and a 480 nm control laser. They will be used to go to the Rydberg state with a two-photon excitation.
To observe Rydberg blockade effect, the linewidth of the lasers has to be lower than the interaction-induced energy shifts between Rydberg atoms (of order MHz). This effect is necessary to achieve the one dimensional geometry of the Rydberg excitation in chapter 4. Therefore, the 480 nm laser was frequency stabilized using the Pound Drever Hall method (see section 2.3.1). An estimated linewidth of about 3 kHz was achieved. This is comparable to a more detailed measurement, done by Florian Pausenwang before the move to a new lab [25]. The probe laser has already been stabilized [19] [17].
For both lasers acousto-optical modulators were implemented to allow pulse shaping of a duration of $\sim 1\,\mu s$. Rise times of (73.9 ± 0.6) ns were measured for the probe laser and (107.6 ± 0.6) ns for the control laser (see section 2.2 and section 2.3.2).

The second part was to plan and build the optics setup for the excitation of Rydberg atoms in a one-dimensional geometry. To achieve that, the laser beams used for Rydberg excitation are tightly focused such that the beam waist at the focus is below the blockade radius and Rydberg atoms can be excited only along the optical axis (see section 4.2). For that, the light from the two laser at 480 nm and 780 nm is used as two counter-propagating beams on a common optical axis for the excitation of ^{87}Rb Rydberg atoms (see section 4.3).
To characterize the performance, a test setup was built in section 4.4. For this, suitable single mode fibers with the best beam profile were selected in section 4.4.1 to ensure that the beam profile of the probe beam at the focus is as close as possible to the expected profile.
Subsequently, the optics from Figure 4.5 were installed one after the other. After each new optic, the beam profile was measured at the focus to ensure that the beam profile matched the expected dimensions of $w_0 \approx 8\,\mu m$ radius at the focus of the probe beam and that there are no aberrations at the focus.
The beam radius meets expectations. Furthermore, the beam profile at the focus is very close to that of an ideal Gaussian profile and no significant aberrations are visible (see Figure 4.15).

By adjusting the position of the second lens with micrometer precision, it was possible to achieve a

coupling efficiency of the probe beam back into the fiber of about 87 % . Furthermore, the coupling efficiencies in both beam propagation directions matched within the measurement accuracy. Thus, it can be assumed that the foci for both directions are at the same location and probe beams can therefore be used from both directions (see section 4.4.1). For the coupling into the separate arms to send the probe light to photon detectors, a coupling efficiency of about 85 % could be achieved with self-built fiber couplers (see section 4.4.1). Finally, the control beam was successfully overlapped with the probe beam (see section 4.4.2).

To measure the probe and control beams at the focus, the commercial *Arducam MT9J001* with a pixel size of 1.67 µm x 1.67 µm [15] was used. In chapter 3 it was explained how to calibrate the camera so that it can be used for beam characterization of small beams with diameters of a few micrometers despite an undesirable Bayer pattern (see section 3.2). Furthermore, software was written to use the camera for alignment of laser beams and optics (see section 3.3).

The next step is to characterize the setup with all optics that will be used in the experiment (see Figure 4.5 for that). This will be done by Valerie Leu. Subsequently, the setup must be built around the science chamber. If this works, the first Rydberg atoms can be excited.

APPENDIX A

Appendix

A.1 Useful tools - microscope

A microscope was set up to measure the beam. An objective corrected to infinity with NA = 0.45 was used for this purpose. In figure A.3 one can see the setup, the components are mounted in the tube to ensure stability and good alignment. A $f = 200\,\text{mm}$ achromat was used as a tube lens. For imaging, the *Arducam MT9J001* was used. In Figure A.4 one can see the setup used to measure the beam at focus. The ruler ensures that the microscope does not slip. The microscope is connected to a construction of three translation stages at the front. The large translation stage is intended to measure the beam around the focus. The other two are used to align the microscope. It turned out that otherwise it is extremely difficult to find the enlarged beam at all. Therefore the reflection of the beam at an aperture on the lens was observed with a second camera. Figure A.1(a) shows the reflections before the microscope is aligned, Figure A.1(b) shows the reflections with the microscope aligned. After alignment, the beam is always visible on the camera. To determine the magnification of the microscope, the *USAF 1951* test target was used. This was used to take the image shown in Figure A.2(a). With the help of the data sheet, the magnification can be determined.

Later, the sensor of the Arducam was also examined with the microscope. Since the sensor is not transparent, a setup was used that works with reflected light. Figure A.5 shows the setup. A beam splitter and a flashlight were sufficient. Here, one has to be very patient, because the contrast is relatively low, it can help to move the flashlight until one gets the best contrast. This was also used to calculate the magnification, the values agrees with the values calculated with the test target. An image of the sensor is shown in Figure A.6.

In section 4.4.1 the measured beam radius is smaller than expected. The assumption is that this is a systematic error due to calculating the magnification with white light. To test this hypothesis one could use a colour camera to image the test target. If then one sees chromatic aberrations at the edges of the bars one could estimate the difference in magnification for different wavelengths and see if this matches with the difference in the measured beam radius from section 4.4.1.

One could also try to measure the magnification with 780 nm light. With the available laser light, however, this did not work here.

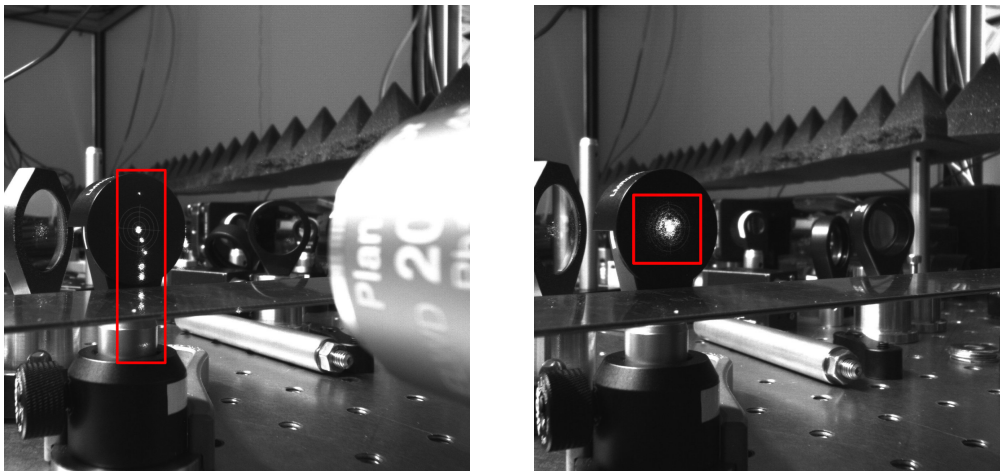

(a) not aligned (b) aligned

Figure A.1: by looking at the reflections, with an IR sensitive camera, from all the lenses inside the objective one can align the microscope with the translation stages

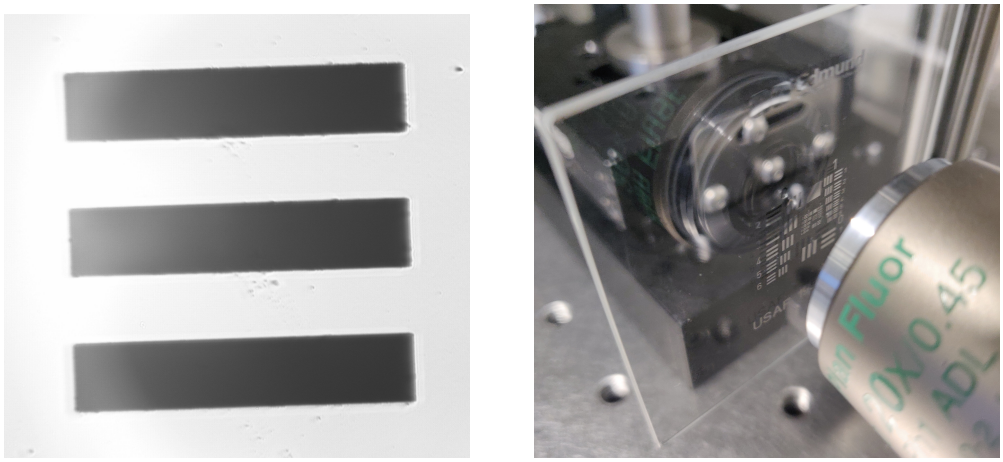

(a) used to calculate magnification (b) *USAF 1951* test target

Figure A.2: the left image was taken with the microscope to calculate the magnification, the images shows row 2 and column 4 from the datasheet

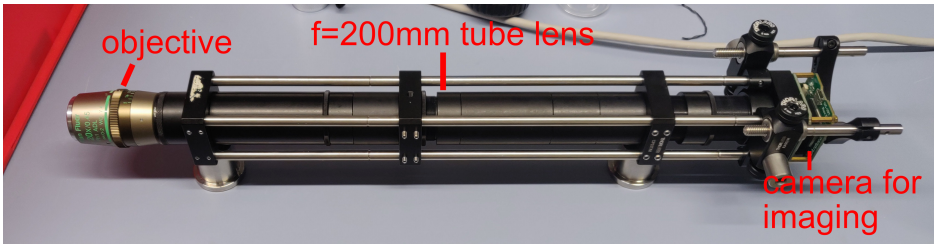

Figure A.3: Setup of microscope with infinty corrected objective and tube lens inside a tube/cage system to guarantee stability and good alignment

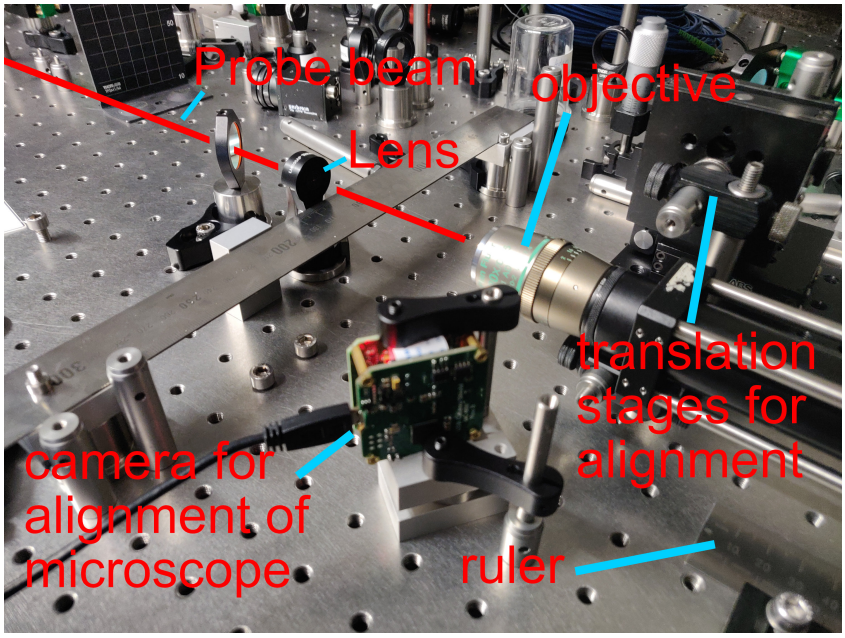

Figure A.4: Setup to measure the probe beam around the focus. The microscope can be moved along all three axis with the translation stages (for alignment and to move along the optical axis of the probe beam). The camera is to look at the reflections from the objective to align the microscope. The aperture is removed when taking images of the beam

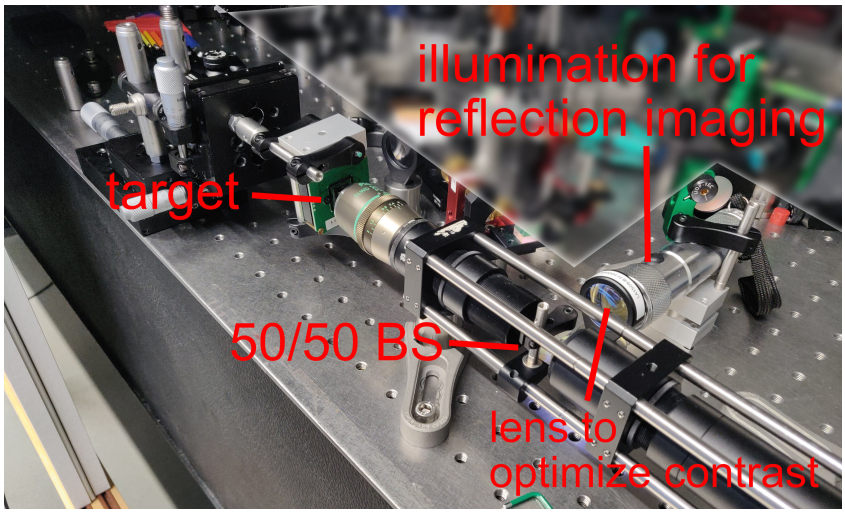

Figure A.5: Setup to image the sensor of the Arducam. The BS allow to shine light onto the target. One cann then image the reflections from the target. This allows to look at opaque targets but with low contrast. The lens is there to optmize the contrast by changing the incident light beam that hits the target

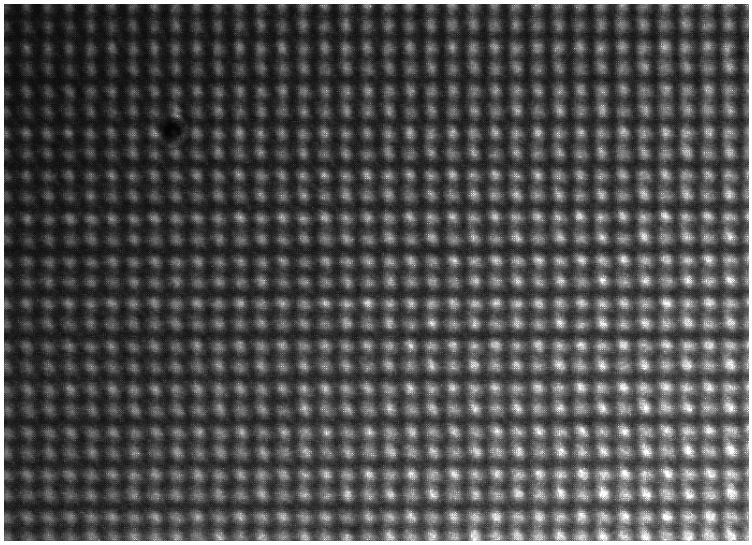

Figure A.6: Image of the sensor of the Arducam, taken with the microscope and another Arducam, the image was rotated and the contrast was enhanced

A.2 Placement of second lens to optimize the coupling efficiency

This is a more detailed description of the procedure to place the second lens that collimates the beam again.
In the theoretical ideal case the beam profile of both collimators would be identical and in both cases the beam would be collimated as good as possible. This is not the case in reality, but it is still the first and easiest choice to collimate and recouple the beam with the second lens. Now there are two challenges: The lens must be positioned on the optical axis so that the beam is collimated. Furthermore, the height of the lens and the horizontal position must fit so that the beam profile is not distorted. The height of the lens is the easiest to adjust. For this purpose the camera was placed behind the second lens. Then a picture of the beam without the lens was taken with the software (see 3.3). After that the lens was put in and the height was adjusted so that the vertical beam profiles with and without lens coincide. The setup for this can be seen in Figure A.7. Then the construction of figure A.8 was built. With this construction the lens can be moved parallel and orthogonal to the optical axis. At the same time the holder prevents a tilting of the lens. Next, the shear-plate interferometer was used to collimate the beam. The setup for this is shown in Figure A.9. When the beam is collimated, the interference pattern of the interferometer is parallel to the beam; when the beam is divergent or convergent, it is not. Figure A.10(b) shows the beam before it was collimated. With the translation stage, the position could then be adjusted until the beam was collimated.Figure A.10(a) shows the interference pattern of the collimated beam. Next, the horizontal position of the lens was adjusted. For this simply two apertures and a power meter were used. The position was adjusted with the other translation stage. Now the beam was coupled into the fiber for the first time. After optimizing the coupling, values in the order of 60 % to 70 % coupling efficiency were achieved. Now it is important that the lens is not yet fixed mounted. Next, the lens was moved with the translation stage along the optical axis in steps of 50 µm. After each shift, the coupling was optimized. Thus a coupling efficiency of about 87 % could be achieved (of course one can choose smaller steps, but this will

increase the time needed). One problem is that the lens slips when it is mounted tightly, which can be seen clearly on the camera. Therefore in figure A.9 the camera was positioned and a picture of the beam was taken after the optimization of the coupling. Then, the mounting screw was tightened. On the camera one can see how the beam profile shifts, with the translation stages one can correct the position while tightening the screw. After the lens was mounted, a coupling efficiency of about 87 % could be achieved.

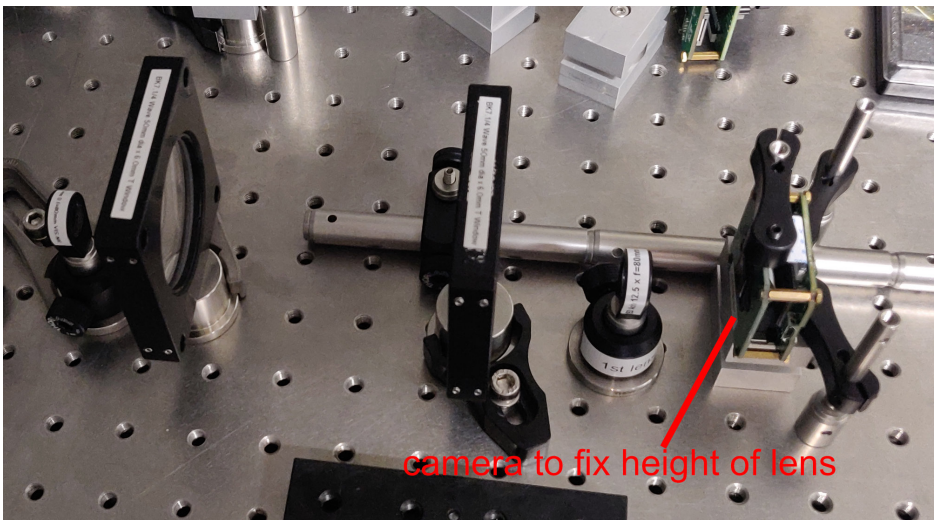

Figure A.7: Setup with Arducam to adjust the height of the second lens

A.3 Arducam

A.3.1 Distortion of beam profile by the camera

In the bottom row of Figure A.11 one can see the normalized difference of both measurement series where the second measurement series was rotated back by 90 degrees to compensate for the 90 degree rotation of the camera. If the ellipticity was a property of the beam, the difference should disappear almost completely (apart from random fluctuations). However, a similar pattern is seen in all five beams, this pattern matches the interference pattern which is clearly visible further away from the focus. (Stretching in one diagonal and compression in the other diagonal) Therefore, it seems that the camera is slightly distorting the beam, causing the ellipticity.

This is generally a good way to distinguish interference effects caused by the camera from actual artifacts in the beam profile. Since the interference pattern remains oriented the same relative to the orientation of the camera, subtracting two measurements (with 90 degree rotation of the camera for one measurement) can characterize the distortion of a beam by the camera.

A.3.2 Code of software for alignment and beam profiling

The complete repository with all required files is on the group's SVN. The name of the program is *beam_matching_final.py*. Check the code for required packages that have to be installed and make

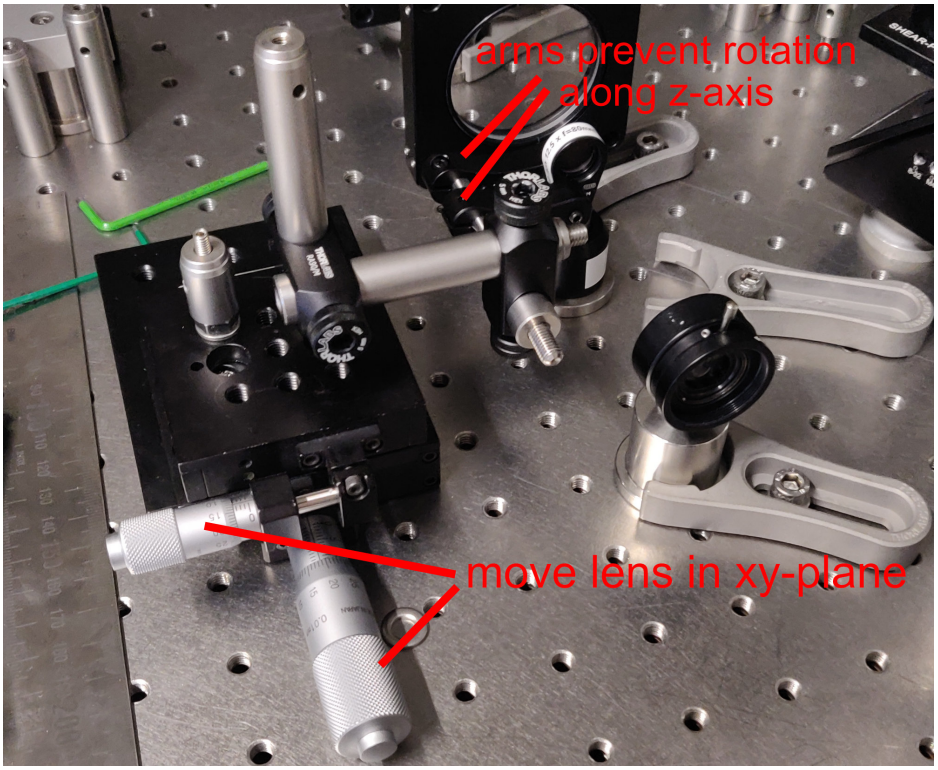

Figure A.8: Setup to move the lens on the table with two translation stages while preventing a rotation along the z-axis

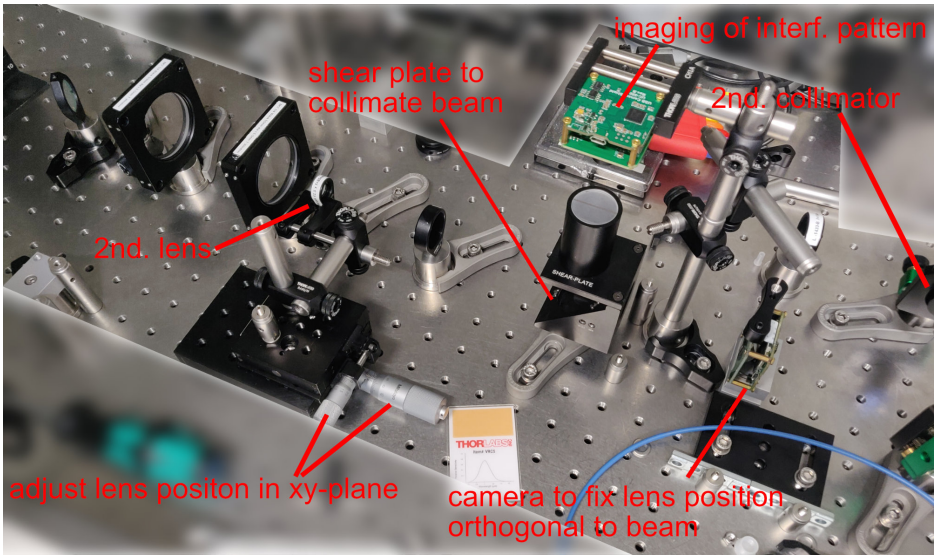

Figure A.9: Setup with shear plate and second camera to fix horizontal position of lens to mount the lens on the table

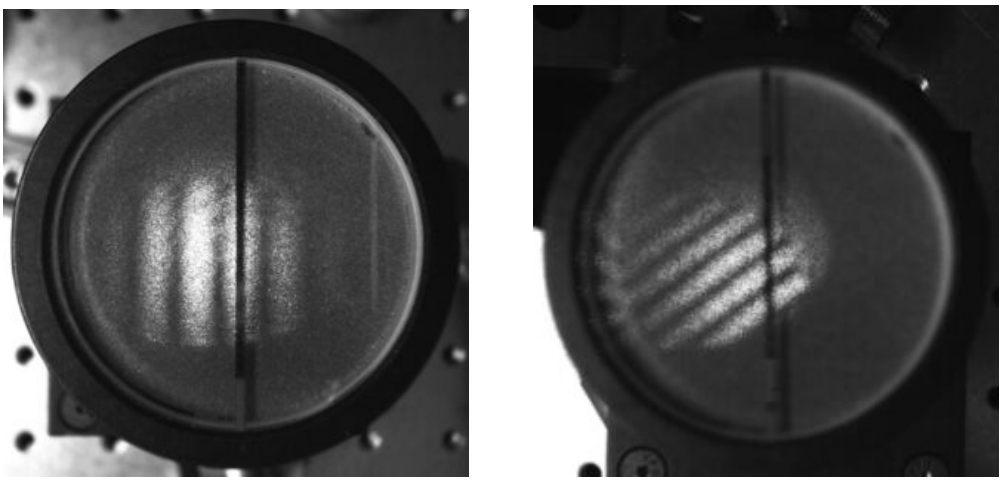

(a) Collimated beam (b) Uncollimated beam

Figure A.10: Interference pattern of shear plate of probe beam, captured with camera

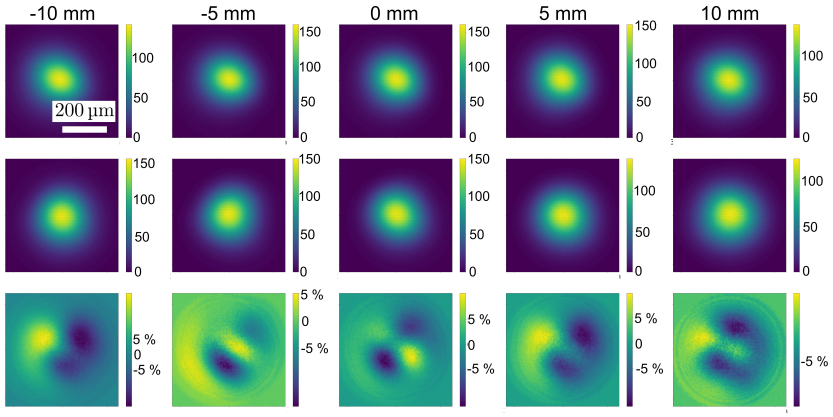

Figure A.11: Images of the probe beam around the focus after the first lens and the dichroic mirror, the pictures were taken with the microscope setup, the top row is with camera in normal position, the camera is turned 90 degree in the second row, the third row shows the normalized difference between the top row and the second row rotated back 90 degree. The scale is the actual scale of the image on the sensor and not the scale before the magnification. The colorbars show the values of the pixels. The position above the pictures is the position of the camera along the optical axis relative to the focus position of the beam.

sure that the python library from *Arducam* is installed.
The program will run with the following command:

```
python beam_matching_final.py {additional_arguments}
```

If the *MT9J001* is used with the *USB2.0_UC-391_Rev.D* shield, the program will run directly. If another shield is used, the path to the config file has to be specified. One has to use a config file with the max resolution of 3664x2748 and 8bit mode:

```
python beam_matching_final.py -f {path_to_config_file} {
    other_additional_arguments}
```

If an existing image is used for reference, the programm will run with the following command:

```
python beam_matching_final.py -c {path_to_reference_image} {
    other_additional_arguments}
```

Check if the orientation of the reference image is the same as the orientation of the live image. Possibly, one hast to flip the orientation of the image.
Make sure to keep the exposure value above 200, otherwise the camera does not work in the intended way. Check the code for keyboard shortcuts for saving images and other things. The calibration from section 3.2 is already used in the software.
If one wants to add more functionalities, here are two ideas:

- do a live gaussian fit to the intensity profiles and display it
- possibility to store an array of multiple images you can use to compare to live image

Bibliography

[1] F. Arute et al., *Quantum supremacy using a programmable superconducting processor*, Nature **574** (2019) 505 (cit. on p. 1).

[2] M. Saffman, T. G. Walker and K. Mølmer, *Quantum information with Rydberg atoms*, Rev. Mod. Phys. **82** (3 2010) 2313, URL: https://link.aps.org/doi/10.1103/RevModPhys.82.2313 (cit. on p. 1).

[3] J. A. Sedlacek et al., *Microwave electrometry with Rydberg atoms in a vapour cell using bright atomic resonances*, Nature physics **8** (2012) 819 (cit. on p. 1).

[4] H. Fan et al., *Atom based RF electric field sensing*, Journal of Physics B: Atomic, Molecular and Optical Physics **48** (2015) 202001, URL: https://dx.doi.org/10.1088/0953-4075/48/20/202001 (cit. on p. 1).

[5] F. Bariani, J. Otterbach, H. Tan and P. Meystre, *Single-atom quantum control of macroscopic mechanical oscillators*, Phys. Rev. A **89** (1 2014) 011801, URL: https://link.aps.org/doi/10.1103/PhysRevA.89.011801 (cit. on p. 1).

[6] R. Stevenson, J. ř. Miná ř, S. Hofferberth and I. Lesanovsky, *Prospects of charged-oscillator quantum-state generation with Rydberg atoms*, Phys. Rev. A **94** (4 2016) 043813, URL: https://link.aps.org/doi/10.1103/PhysRevA.94.043813 (cit. on p. 1).

[7] M. Gao, Y.-x. Liu and X.-B. Wang, *Coupling Rydberg atoms to superconducting qubits via nanomechanical resonator*, Phys. Rev. A **83** (2 2011) 022309, URL: https://link.aps.org/doi/10.1103/PhysRevA.83.022309 (cit. on p. 1).

[8] A. D. O'Connell et al., *Quantum ground state and single-phonon control of a mechanical resonator*, Nature **464** (2010) 697 (cit. on p. 1).

[9] Y. Chu et al., *Quantum acoustics with superconducting qubits*, Science **358** (2017) 199, URL: https://www.science.org/doi/abs/10.1126/science.aao1511 (cit. on p. 1).

[10] E. Urban et al., *Observation of Rydberg blockade between two atoms*, Nature Physics **5** (2009) 110 (cit. on pp. 1, 23).

[11] T. Nirrengarten et al., *Realization of a Superconducting Atom Chip*, Phys. Rev. Lett. **97** (20 2006) 200405, URL: https://link.aps.org/doi/10.1103/PhysRevLett.97.200405 (cit. on p. 1).

[12] O. Firstenberg, C. S. Adams and S. Hofferberth, *Nonlinear quantum optics mediated by Rydberg interactions*, Journal of Physics B: Atomic, Molecular and Optical Physics **49** (2016) 152003, URL: https://dx.doi.org/10.1088/0953-4075/49/15/152003 (cit. on p. 2).

[13] T. Peyronel et al., *Quantum nonlinear optics with single photons enabled by strongly interacting atoms*, Nature **488** (2012) 57 (cit. on p. 2).

[14] H. Gorniaczyk, C. Tresp, J. Schmidt, H. Fedder and S. Hofferberth, *Single-Photon Transistor Mediated by Interstate Rydberg Interactions*, Phys. Rev. Lett. **113** (5 2014) 053601, URL: https://link.aps.org/doi/10.1103/PhysRevLett.113.053601 (cit. on p. 2).

[15] *Arducam 10MP MT9J001 Monochrome CMOS 1/2.3 Camera Module*, URL: https://www.arducam.com/product/arducam-cmos-mt9j001-1-2-3-inch-10mp-monochrome-camera-module/ (visited on 16/07/2023) (cit. on pp. 2, 11, 40).

[16] D. Meschede, *Optik, Licht und Laser*, 3rd ed., Vieweg+Teubner, 2008 (cit. on pp. 2, 4, 8, 22).

[17] V. Mauth, *Realization of a 87Rb magneto-optical trap*, Bachelor Thesis: University of Bonn, 2023 (cit. on pp. 3, 4, 39).

[18] Daniel A. Steck, *Rubidium 87 D Line Data*, 2001 (cit. on p. 3).

[19] J. Gamper, *Frequenzstabilisierung zur Laserkühlung von Rubidium*, Bachelor Thesis: University of Bonn, 2022 (cit. on pp. 4, 39).

[20] Y. V. Gulyaev, M. A. Kazaryan, Y. M. Mokrushin and O. V. Shakin, *Acousto-Optical Laser Systems for the Formation of Television Images*, CRC Press, 2019 (cit. on p. 5).

[21] *AOMO 3080-122 Datasheet*, URL: https://cdn.sanity.io/files/8jt7x1sz/production/04f10616fa044262d8b6594fe13c08e3ce9f74ac.pdf (visited on 02/08/2023) (cit. on p. 5).

[22] E. D. Black, *An introduction to Pound–Drever–Hall laser frequency stabilization*, American Journal of Physics **69** (2001) 79, ISSN: 0002-9505, eprint: https://pubs.aip.org/aapt/ajp/article-pdf/69/1/79/10115998/79_1_online.pdf, URL: https://doi.org/10.1119/1.1286663 (cit. on p. 6).

[23] T. Kawanishi, *Electro-optic Modulation for Photonic Networks*, Springer, 2022, URL: https://doi.org/10.1007/978-3-030-86720-1 (cit. on p. 6).

[24] I. D. Díaz-Rodríguez, S. Han and S. P. Bhattacharyya, *Analytical Design of PID Controllers*, Springer, 2019, URL: https://doi.org/10.1007/978-3-030-18228-1 (cit. on p. 7).

[25] F. Pausenwang, *Aufbau, Optimierung und Charakterisierung von frequenzstabilisierten Lasersystemen*, Bachelor Thesis: University of Bonn, 2022 (cit. on pp. 8, 9, 39).

[26] M. González-Cardel, P. Arguijo and R. Uribe, *Gaussian beam radius measurement with a knife-edge: A polynomial approximation to the inverse error function*, Applied optics **52** (2013) 3849 (cit. on p. 11).

[27] R. C. Montaña, "Encoding Color: Between Perception and Signal", *Visualizing Achromatic Knowlegde*, ed. by B. B. von Wülfingen, Berlin, Boston: De Gruyter, 2019 99, ISBN: 9783110605211, URL: https://doi.org/10.1515/9783110605211-007 (cit. on p. 11).

[28] *chessboard noise in MT9J001*, URL: https://github.com/ArduCAM/ArduCAM_USB_Camera_Shield/issues/84 (visited on 17/07/2023) (cit. on pp. 12, 14).

[29] *MT9J003 Registers*, URL: https://www.arducam.com/downloads/modules/industrial/MT9J003_RR_A.pdf (visited on 18/07/2023) (cit. on pp. 13, 14, 16).

[30] *DIPlib-OpenCV interface module*, URL: https://diplib.org/diplib-docs/dip_opencv_interface.html#:~:text=OpenCV%5C%20recognizes%5C%20the%5C%20following%5C%20types,bit%5C%20and%5C%2064%5C%2Dbit%5C%20floats. (visited on 09/08/2023) (cit. on p. 14).

[31] *1/2.3-Inch 10Mp CMOS Digital Image Sensor*, URL: http://www.altavision.com.br/Arquivos/Sensor/MT9J003_datasheet.pdf (visited on 18/07/2023) (cit. on pp. 14–16).

[32] *Software SDK and API for Python*, URL: https://docs.arducam.com/USB-Industrial-Camera/Quick-Start-Guide/Software-SDK-and-API-for-Windows/Software-SDK-and-API-for-Python/ (visited on 07/08/2023) (cit. on p. 16).

[33] *10MP MT9J001/MT9J003*, URL: https://www.arducam.com/doc-old/camera-breakout-board/10mp-mt9j001-mt9j003/ (visited on 17/07/2023) (cit. on p. 19).

[34] S. A. Self, *Focusing of spherical Gaussian beams*, APPLIED OPTICS **22** (1983) 658 (cit. on p. 23).

[35] *RS1LM - Ø25 mm Laminated Post Spacer, 1 mm Thick, Pack of 5*, URL: https://www.thorlabs.com/thorproduct.cfm?partnumber=RS1LM (visited on 22/07/2023) (cit. on p. 29).

[36] *Refractive index database*, URL: https://refractiveindex.info/?shelf=glass&book=BK7&page=SCHOTT (visited on 10/08/2023) (cit. on p. 34).

[37] D. A. Page, *Interferometry Handbook of Optical Metrology*, Toru Yoshizawa, 2015 (cit. on p. 36).

[38] *SI050 - Shearing Interferometer with a 2.5-5 mm Beam Diameter Shear Plate*, URL: https://www.thorlabs.com/thorproduct.cfm?partnumber=SI050#ad-image-0 (visited on 09/08/2023) (cit. on p. 36).